Materials Today Bio 28 (2024) 101180

Contents lists available at ScienceDirect

Materials Today Bio

journal homepage: www.journals.elsevier.com/materials-today-bio

A photothermal responsive system accelerating nitric oxide release to enhance bone repair by promoting osteogenesis and angiogenesis

Yannan Cheng [a,1], Yuanfang Huo [b,1], Yongle Yu [a,1], Ping Duan [a], Xianzhen Dong [b], Zirui Yu [a], Qiang Cheng [b], Honglian Dai [b,c,**], Zhenyu Pan [a,*]

[a] Department of Orthopedics Trauma and Microsurgery, Zhongnan Hospital of Wuhan University, Wuhan, 430071, China
[b] State Key Laboratory of Advanced Technology for Materials Synthesis and Processing, Wuhan University of Technology, Biomedical Materials and Engineering Research Center of Hubei Province, Wuhan, 430070, China
[c] Shenzhen Research Institute of Wuhan University of Technology, Shenzhen, 518000, China

ARTICLE INFO

Keywords:
Nitric oxide
Nanoparticles
Injectable hydrogel
Osteogenesis
Angiogenesis

ABSTRACT

Managing bone defects remains a formidable clinical hurdle, primarily attributed to the inadequate orchestration of vascular reconstruction and osteogenic differentiation in both spatial and temporal dimensions. This challenge persists due to the constrained availability of autogenous grafts and the limited regenerative capacity of allogeneic or synthetic bone substitutes, thus necessitating continual exploration and innovation in the realm of functional and bioactive bone graft materials. While synthetic scaffolds have emerged as promising carriers for bone grafts, their efficacy is curtailed by deficiencies in vascularization and osteoinductive potential. Nitric oxide (NO) plays a key role in revascularization and bone tissue regeneration, yet studies related to the use of NO for the treatment of bone defects remain scarce. Herein, we present a pioneering approach leveraging a photothermal-responsive system to augment NO release. This system comprises macromolecular mPEG-P nanoparticles encapsulating indocyanine green (ICG) (NO-NPs@ICG) and a mPEG-PA-PP injectable thermosensitive hydrogel carrier. By harnessing the synergistic photothermal effects of near-infrared radiation and ICG, the system achieves sustained NO release, thereby activating the soluble guanylate cyclase (SGC)-cyclic guanosine monophosphate (cGMP) signaling pathway both in vitro and in vivo. This orchestrated cascade culminates in the facilitation of angiogenesis and osteogenesis, thus expediting the reparative processes in bone defects. In a nutshell, the NO release-responsive system elucidated in this study presents a pioneering avenue for refining the bone tissue microenvironment and fostering enhanced bone regeneration.

1. Introduction

Bone, a mineralized connective tissue, serves as the fundamental scaffold of the human body, crucial for support, protection, and movement, while also possessing a distinctive self-repair capability [1,2]. However, instances of bone defects resulting from traumatic injuries, tumors, chronic inflammation, bone necrosis, and osteoporosis can surpass the bone's inherent healing capacity, necessitating supplementary therapeutic interventions that significantly influence patients' long-term prognoses [3]. Despite autogenous bone grafting being considered the gold standard for such treatments, its utilization is constrained by inherent limitations, including susceptibility to surgical infection, limited availability, and prolonged surgical duration [4]. Consequently, the imperative persists for the exploration of alternative treatments to bone grafting that exhibit broader clinical applicability.

The realm of bone tissue engineering has witnessed substantial attention in recent decades, with sustained research endeavors aimed at refining bone tissue regeneration through biomaterial strategies [5–7]. Biomaterials assume a pivotal role as scaffolds for cell adhesion and growth, profoundly shaping the tissue microenvironment [8,9]. Given the highly vascularized nature of bone tissue, the interplay between vascular growth and osteogenesis emerges as a crucial facet within the skeletal system [10,11]. Following bone tissue injury, activation of signaling pathways such as VEGFA and extracellular matrix components

* Corresponding author.
** Corresponding author.
E-mail addresses: daihonglian@whut.edu.cn (H. Dai), zn000382@whu.edu.cn (Z. Pan).
[1] Yannan Cheng, Yuanfang Huo and Yongle Yu are co-first authors.

https://doi.org/10.1016/j.mtbio.2024.101180
Received 30 March 2024; Received in revised form 27 July 2024; Accepted 3 August 2024
Available online 10 August 2024

facilitates the infiltration of nascent vessels [12]. The orchestration of new blood vessel formation proves indispensable for bone repair and regeneration, as it not only guides the migration of mesenchymal stem cells but also fosters their osteogenic differentiation, culminating in bone formation [13]. Hence, the development of bone graft scaffolds endowed with angiogenic and osteogenic properties represents a promising avenue for augmenting current bone regeneration modalities, thereby expediting the healing response and tissue regeneration process.

Nitric oxide (NO) emerges as an endogenous multifunctional signaling molecule generated by epithelial cells, vascular endothelial cells, macrophages, and inflammatory cells, participating in a spectrum of physiological and pathological processes such as vasodilation, neural regulation, and tumorigenesis [14–18]. Moreover, empirical evidence underscores the role of exogenous NO in promoting the proliferation and differentiation of osteoblasts to mitigate osteoporosis [19–22]. The cyclic guanosine monophosphate/protein kinase G (cGMP/PKG) signaling pathway is a critical intracellular signal transduction mechanism, essential for the regulation of various physiological systems throughout the body. NO regulates vascular and bone regeneration by activating the soluble guanylate cyclase (SGC) to initiate the cGMP/PKG pathway [7,23]. Research indicates that the NO/cGMP/PKG signaling pathway is pivotal in promoting osteoblast proliferation and differentiation, enhancing their resistance to apoptosis, and facilitating the vascularization of bone endothelial cells [24,25]. The mechanical loading effects on the skeletal system are also contingent upon the involvement of the NO/cGMP/PKG pathway. Notably, PKG, via the Wnt/β-catenin pathway, drives bone acquisition and adaptation to mechanical loading in male mice [26]. Additionally, cGMP agonists can reverse the reduced expression of VEGFA and BMP2/4 in the bones of diabetic mice, thereby ameliorating the diminished osteoblast population, collagen deposition, and microvascular formation in bone defect areas [27]. Collectively, the expression of the NO/cGMP/PKG pathway is essential for bone remodeling.

Nonetheless, the transient nature of NO in tissues (with a half-life of approximately 5 s) and its constrained diffusion radius (ranging from 40 to 200 μm) pose challenges in addressing the protracted, gradual process of bone repair [28]. S-nitrosothiols (RSNOs) represent a class of photosensitive NO donors purported to sequester and transport NO within the body for prompt release upon exposure to Ultraviolet light or heat stimulation [29,30]. Given this, the construction of a photothermally induced RSNO delivery system holds promise for effectively stimulating angiogenesis and osteoinduction.

In the present investigation, we devised a system employing ultrasound self-assembly to encapsulate indocyanine green (ICG) nitric oxide donor nanoparticles, termed poly (ethylene glycol methacrylate)-poly (nitrosomethane-polyethylene glycol) nanoparticles (NO-NPs@ICG), subsequently incorporating them into a thermosensitive hydrogel [methoxy poly (ethylene glycol)-poly(acrylic acid)-poly(phenylalanine), (mPEG-PA-PP)], thereby facilitating injectability and NO-releasing capabilities. Subsequent utilization of near-infrared light or stimuli promoting NO release effectively bolstered angiogenesis and bone repair (Fig. 1). In summary, this investigation endeavors to unveil a novel bone repair strategy predicated on a photothermal effect-induced NO release response system.

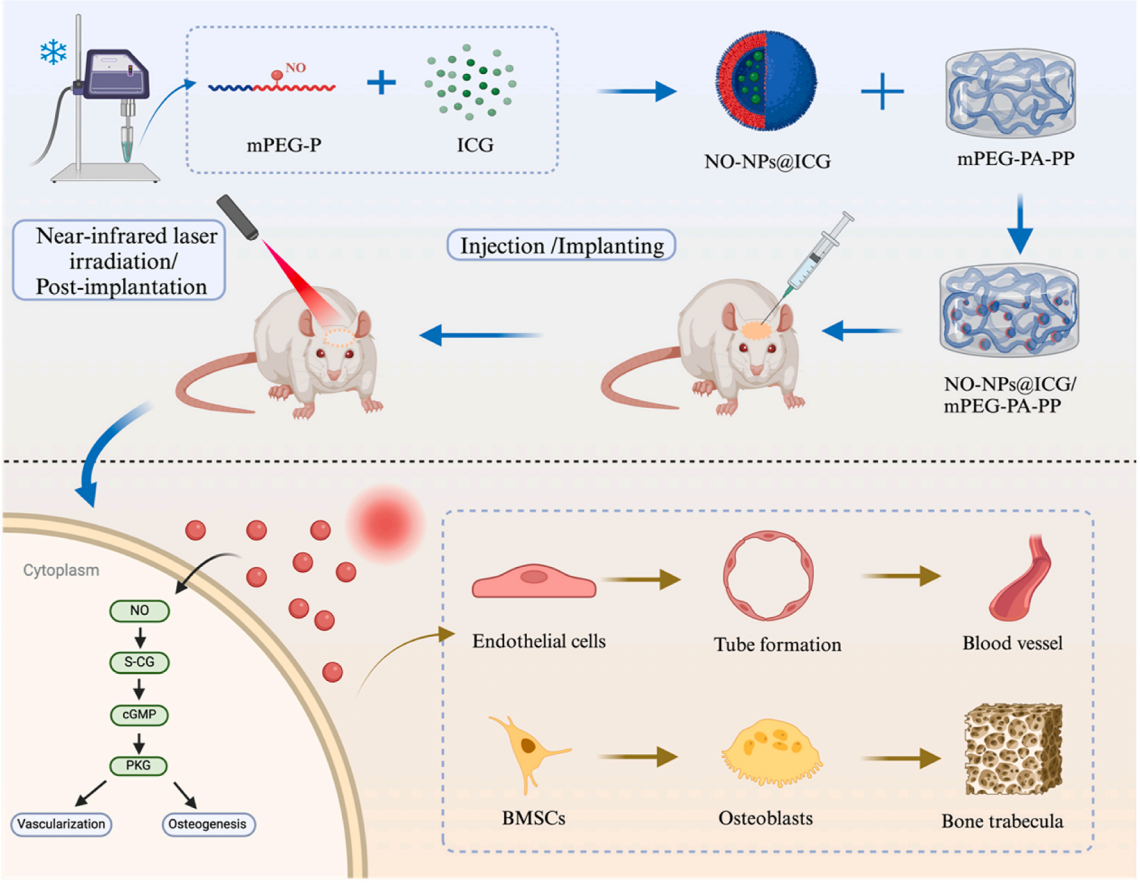

Fig. 1. Schematic representation of the construction of a response system for accelerating NO release and promotion of bone repair. The mPEG-P (MSNO-EG) and ICG are combined to form NO-NPs@ICG nanoparticles through ice bath and sonication. These are incorporated into a thermosensitive hydrogel and implanted into bone defects. Photothermal enhancement releases NO, activating the cGMP/PKG pathway to enhance angiogenesis and osteoblast differentiation, thus speeding up bone repair. (For interpretation of the references to color in this figure legend, the reader is referred to the Web version of this article.)

2. Materials and methods

2.1. Materials

Methoxypolyethylene glycols (mPEG, Mn = 5000 and Mn = 2000) was obtained from Sigma-Aldrich. Ethylene glycol (EG), mercaptosuccinic acid (MS), p-toluenesulfonic acid monohydrate (PTSA), ethylene diamine tetraacetic acid (EDTA), and triphosgene purchased from Shanghai Aladdin Biochemical Technology Co., Ltd. Hexyl hydride, anhydrous ether, $CHCl_3$, KOH, NH_4Cl, aqueous ammonia, tetrahydrofuran (THF), and acetone obtained from Sinopharm Chemical Reagent Co., Ltd. Tert-butyl nitrite purchased from Tokyo Chemical Industry (TCI, Shanghai). NO detection kit (S0021S) was obtained from Beyotime.

2.2. Synthesis of mPEG-P(MS-EG) polymers

Add mPEG (2 g, Mn = 5000), PTSA (0.16 g), EG (372 μL), MS (1 g), and EDTA (0.16 g) to the reaction bottle (100 mL). Then this system was placed in a nitrogen environment and reacted for 8 h at 120 °C. After the reaction was completed, acetone was poured into the reaction bottle while hot to dissolve the product. Subsequently, the above solution was poured into ice ether to settle, repeated three times. Then, mPEG-P(MS-EG) was obtained.

2.3. Synthesis of mPEG-P(MSNO-EG) polymers

0.5 g mPEG-P(MS-EG) was dissolved in 20 mL methanol, then 2 equivalents of tert-butyl nitrite were added. After 20 min, 5 mL $CHCl_3$ was added to the reaction bottle. Until the reaction system turned red, the reaction ended. The liquid was poured into precooled ether to settle. Then mPEG-P(MSNO-EG) was obtained.

2.4. Preparation of NO-NPs@ICG/NO-NPs/Pre-NPs

Firstly, the reaction bottle containing 4 mL PBS and 1 mg ICG was placed in an ultrasound machine (Scientz-IID, Xinzhi, China). 10 mg mPEG-P(MSNO-EG) was dissolved in 150 μL methanol. Then mPEG-P (MSNO-EG) solution was added into PBS and continued ultrasound for 10 min at 0 °C. After that, methanol was removed by vacuum drying. The preparation methods of NO-NPs and Pre-NPs were the same as above, but ICG was not added to PBS.

2.5. Synthesis of mPEG-PA-PP polymers

1 g mPEG-NH_2 was melted under vacuum at 80 °C for 2 h. Then 200 mL DMF was added to obtain mPEG-NH_2 solution. After 0.69 g alanine NCA was added for 3 days, 0.48 g phenylalanine NCA was added to react in an anaerobic environment for 3 days. After the reaction was completed, the solution was poured into n-hexane to settle.

2.6. Characterization

^1H NMR of each reaction step product was obtained by the Avance III HD 500 MHz NMR spectrometer (Bruker, Germany). Fourier transform infrared spectroscopy (FTIR, Vertex 80V spectrometer, Bruker, Germany), with a testing range of 400–4000 cm^{-1}, was used to test the functional groups of mPEG-P(MS-EG) and mPEG-P(MSNO-EG). The dose-response relationship between –SNO and NO-NPs was measured by the visible UV spectroscopy (UV-1900i, Ishizu, Japan). STA449F3 comprehensive thermal analyzer (DSC/DTA-TG) used to obtain thermogravimetric spectrum of mPEG-P(MS-EG) and mPEG-P(MSNO-EG). JEM-1400Plus transmission electron microscopy (TEM, JEOL, Japan) was used to obtain the microscopic morphology of nanoparticles. DLS (the Nano ZS, Malvern Instruments, UK) was used to test the mean hydrodynamic diameter and size distribution of nanoparticles. The nanoparticles (2 mg/mL) were filtered by a pore size of 0.45 μm filter for DLS measurement.

To evaluate the release ability of NO-NPs@ICG, we prepared 5 mL solution of NO-NPs@ICG and NO-NPs (0.5 mg/mL) and irradiated them with near-infrared laser (1 W/cm^2, 808 nm) for 2 min every day. NO-NPs (0.5 mg/mL) were used to detect the concentration of NO at different temperatures and pH values The Griess reagent (S0021S, Beyotime) was used to test NO concentration.

HAAKE Rheological Stress 6000 Rotational Rheometer (Thermo Science, Germany) was used to measure the phase transition temperature and rheological properties of mPEG-PA-PP and ICG@NO-NPs/mPEG-PA-PP hydrogels. The distance between the parallel plate rotor with a diameter of 25 mm and the platform is set to 1 mm. The precursor solution of mPEG-PA-PP or ICG@NO-NPs/mPEG-PA-PP was injected into the gap between the parallel plate rotor and the platform, frequency scanning (10 rad/s, 1 % strain) was performed to obtain the real-time changes of the hydrogel storage modulus (G′) and loss modulus (G). Then reduce the temperature of platform to 37 °C to observe the rheological properties of the hydrogel. JSM-IT200 scanning electron microscopy (SEM, JEOL, Japan) observed the microstructure of hydrogel and electrospun membrane. JSM-IT200 scanning electron microscopy (SEM, JEOL, Japan) was used to obtain the microstructure of hydrogel and electrospun membrane.

2.7. Cell culture and treatment

We purchased human umbilical vein endothelial cells (HUVECs) and bone marrow mesenchymal stem cells (BMSCs) from Procell (WuHan, China). BMSCs were cultured with a maintenance medium consisting of MEMα (Hyclone, USA), supplemented with 10 % FBS (Vivacell, Israel) and 1 % PS (Hyclone, USA). KT5823 was purchased from MedChemExpress. HUVECs was cultured using a specialized culture medium (CM-0122, Procell, China). A humidified environment with 5 % CO_2 at 37 °C was used for the maintenance of all cells. Cells from each group were co-incubated with the corresponding nanoparticles (NPs). And the cells in the NO-NPs@ICG group (ICG, 3 μg/mL) were exposed to 808 nm (1 W/cm^2) laser for 2 min immediately after incubation with the NPs.

2.8. Cell toxicity assay

The Cell Counting Kit-8 (CCK-8) (C0037 Proteintech, China), was diluted in the culture medium to a final concentration of 10 %. Cells were seeded into 96-well plates at a density of 2000 cells per well and allowed to differentiate for periods of 1, 3, and 5 days. Following two PBS washes, 110 μL of the CCK-8 solution was added to each well, and the cells were incubated for an additional 2 h. The optical density (OD) of each well was then quantified at a wavelength of 450 nm.

2.9. Live/dead cell staining and Hoechst 33258 staining

Cell viability was assessed using the live/dead cell staining kit (C2015L, Beyotime, China), following standard protocols. Specifically, cells in the NO-NPs@ICG group were subjected to 808 nm laser irradiation for 2 min, while other groups received alternative treatments. Subsequently, a mixture of calcein AM and propidium iodide (PI) in PBS was prepared and applied to the cells to ensure complete coverage. After the removal of the working solution, the cells were washed three times with PBS before being observed under an inverted fluorescence microscope (IX73, Olympus, Japan).

For the Hoechst33258 staining, cells were treated with the Hoechst Staining Kit (C1017, Beyotime, China). After being subjected to various conditions, the cells were stained with Hoechst33258 in the dark for 20 min within a cell incubator. Following three PBS washes, the cell nuclei morphology was examined using a fluorescent microscope (IX73, Olympus, Japan).

2.10. NO production

NO production was quantified using a specific fluorescent dye, 3-amino, 4-aminomethyl-2′,7′-difluorescein diacetate (DAF-FM DA) (S0019S, Beyotime, China) Cells were pre-incubated with either 100 μM precursor-NPs, 100 μM NO-NPs, or 100 μM NO-NPs@ICG for 12 h. After this, the cells were loaded with 10 μM DAF-FM DA for 30 min at 37 °C in a dark environment, and then gently washed three times with PBS to remove excess dye. The cellular fluorescence was analyzed using a laser scanning confocal microscope (IX73, Olympus, Japan), with the excitation and emission wavelengths set at 495 nm and 515 nm, respectively, to capture the NO signal.

2.11. Quantitative real-time reverse Transcription-polymerase chain reaction (qRT-PCR)

RNA was isolated from samples using TRIzol reagent (R401-01 Vazyme, China) and subsequently reverse transcribed into cDNA using the RevertAid First Strand cDNA Synthesis Kit (K1621, Thermo Fisher Scientific). Quantitative real-time PCR (qPCR) was performed with the ChamQ SYBR qPCR Master Mix kit (Q311, Vazyme, China) on the CFX96 Real-Time PCR system (Bio-Rad), adhering to the instructions provided by the kit manufacturer. The expression levels of genes including *Bmp2, Ocn, Col1a1, Runx2, Sgc, Pkg, SGC, PKG, VEGFA, and CD31* were normalized to the housekeeping gene *β-Actin*. The relative mRNA expression was quantified employing the ΔCt (2-ΔΔCt) method, with primer sequences listed in Fig. S1 of the Supporting Information.

2.12. Western blot analysis

Protein extraction was facilitated by a cell lysis buffer (P0013B, Beyotime, China), with the addition of protease and phosphatase inhibitors, and the protein concentration was ascertained using the BCA Protein Assay Kit (P0009, Beyotime, China). A quantity of 30 μg of protein was resolved through SDS-PAGE and subsequently transferred onto nitrocellulose membranes (Millipore, USA). These membranes underwent a blocking process with a blocking buffer before being incubated with primary antibodies specific to COL1a1 (14695-1-AP, 1:1000, Proteintech), CD31 (11265-1-AP, 1:1000, Proteintech), RUNX2 (12556S, 1:1000, SCT), OCN (ab133612, 1:1000, Abcam), VEGFA (19003-1-AP, 1:1000, Proteintech), BMP2 (A0231, 1:1000, ABclonal), SGC (ab189254, 1:1000, Abcam), PKG (ab97339, 1:1000, Abcam), and β-Actin (81115-1-RR 1:1000, Proteintech), at 4 °C for an overnight period. The membranes were then subjected to incubation with secondary antibodies (1:10000, yamei) for 60 min on a shaker. After a series of washes with the wash solution, the membranes were treated with an Ultra-sensitive chemiluminescence detection kit (yamei, China), and the resulting signals were captured on a VersaDocTM Imaging System (Bio-Rad). The intensity of the bands was quantified utilizing Image J software.

2.13. Wound scratch assay

HUVECs were seeded into six-well plates at a density of 1×10^6 cells per well. Once the HUVECs achieved a confluence of 100 %, a sterile 200 μL pipette tip was employed to create a scratch in the cell monolayer, followed by a gentle wash with PBS to remove any detached cells. The cells were then treated with NPs (100 μM) to assess the impact of NO on wound closure. Specifically, the NO-NPs@ICG group was irradiated with an 808 nm laser for 2 min to activate the NO release. The migration and repopulation of HUVECs were monitored at 0- and 24-h post-scratch, and images were captured using a microscope (IX73, Olympus, Japan). The rate of wound healing was calculated using ImageJv1.8.0 software.

2.14. Endothelial tube formation assay

Matrigel (ABW, 0827045, China) was dispensed into 96-well plates, each well-receiving 50 μL, and the plates were incubated at 37 °C for 60 min to allow the Matrigel to solidify. Groups of HUVECs were co-cultured with NPs (100 μM) for 3 days collected at a density of 20,000 cells per well seeded into Matrigel-coated wells. After an 8-h incubation period, the formation of tube networks was visualized using an microscope (IX73, Olympus, Japan). The quantification of the tube networks was performed using ImageJ v1.8.0 software.

2.15. Immunofluorescence

A 4 % paraformaldehyde solution was applied to 12-well plates that contained BMSCs and HUVECs for 20 min, followed by permeabilization for 10 min with 0.3 % Triton X-100. Subsequently, the cells were blocked with 5 % bovine serum albumin (BSA, Solarbio, China) for 30 min to prevent non-specific binding. Overnight incubation at 4 °C was then carried out with primary antibodies targeting RUNX2 (12556S, 1:1000, SCT), BMP2 (A0231, 1:1000, ABclonal), OCN (ab133612, 1:1000, Abcam), COL1a1 (14695-1-AP, 1:1000, Proteintech), VEGFA (19003-1-AP, 1:1000, Proteintech)), and CD31 (11265-1-AP, 1:1000, Proteintech). The next day, the cells were labeled with secondary antibodies (SA00013-2, SA00013-4, 1:200, Proteintech) for 1 h, FITC-conjugated phalloidin (PF00001, 1:200, Proteintech) for 1 h to visualize the cytoskeleton, and DAPI for 5 min to stain the nucleus. The immunofluorescence was finally imaged using a laser confocal microscope (IX73, Olympus, Japan).

2.16. Alkaline phosphatase assessment and osteogenic mineralization assessment

BMSCs were seeded at a density of 1×10^5 cells per well in 12-well plates. Once the cells reached approximately 70 % confluence, they were treated with an osteogenic induction medium, which was replenished every three days, coinciding with the addition of the novel NPs (100 μM). In the NO-NPs@ICG group, cells were subjected to 808 nm laser irradiation for 2 min during each medium change. The osteogenic induction medium contained 50 mg/mL ascorbic acid (50-81-7, MedChemExpress, China), 10 mM β-Glycerophosphate disodium salt pentahydrate (13408-09-8, MedChemExpress, China), 100 nM dexamethas-one (50-02-2, MedChemExpress, China), 1 % PS, and 10 % FBS.

To assess alkaline phosphatase (ALP) activity, cells were fixed with a 4 % paraformaldehyde solution for 30 min after 7 days of induction, followed by three PBS washes. ALP expression was then detected using the BCIP/NBT Alkaline Phosphatase Chromatography Kit (C3206, Beyotime, China) at room temperature, and the results were visualized under a microscope.

For the analysis of mineralized matrix formation, cells were treated with Alizarin Red S solution (OILR-10001, OriCell, China) after 21 days of induction. Following fixation with 4 % paraformaldehyde for 30 min and three PBS washes, the cells were incubated with the staining solution at room temperature for 30 min. After additional PBS washes, the presence of calcium nodules was examined microscopically.

2.17. The surgical procedure of normal rat calvarial bone defect

The animal experimental protocol, approved by the Central South Hospital Committee of Wuhan University (ZN2023084), involved the administration of 1 % sodium pentobarbital at a dosage of 1 mL per SD rat via intraperitoneal injection. The rats were then prepared for surgery by shaving the hair and disinfecting the skin with 70 % ethanol, followed by a midline sagittal incision. Two 5 mm holes were created in the parietal bones, away from the sagittal suture, to accommodate the injection of the hydrogel with embedded NPs (100 μM) into the defect

area. The periosteum was sutured using absorbable sutures, while the overlying skin was closed with non-absorbable sutures. Rats in the mPEG-PA-PP/NO-NPs@ICG group received 808 nm laser irradiation for 5 min on three occasions per week. Postoperatively, all rats were administered antibiotics for a period of three consecutive days.

2.18. Micro-CT analysis

Following 6 weeks post-surgery, the SD rats were humanely euthanized, and cranial samples were harvested and preserved in a 10 % formalin solution for subsequent analysis. The healing progress within the defect site was initially evaluated using micro-computed tomography (micro-CT) with a SkyScan 1176 scanner (SkyScan, Belgium), employing settings of 65 kV, 385 mA, and a 1 mm aluminum filter. The three-dimensional (3D) reconstruction of the skull was facilitated by Mimic software. To quantify bone and tissue volumes, a cylindrical region of interest (ROI) was defined, and the bone volume to tissue volume ratio (BV/TV), bone mineral density (BMD), Trabecular number (Tb.N) and Trabecular thickness (Tb.Th) were calculated using CT Analyzer software (SkyScan, Belgium).

2.19. Tissue immunochemical staining and immunofluorescence staining

Following a 4-week decalcification process in a formalin-EDTA solution, the specimens underwent a dehydration sequence in ethanol, were embedded in paraffin, and sectioned into 5 μm slices. These sections were then stained with hematoxylin and eosin (HE) as well as Masson's trichrome stain. The vascular distribution across various groups was quantified by measuring the relative expression of CD31 and VEGFA through immunohistochemistry (IHC). The extent of osteogenesis was evaluated by determining the relative expression of RUNX2 and BMP2, also via IHC. The activity of the NO/cGMP signaling pathway was assessed by examining the relative expression of SCG and PKG using immunofluorescence. The tissue sections were examined with a digital scanner (Aperio ScanScope XT; Leica Biosystems, USA), and the resulting data were analyzed using ImageJ software.

2.20. Statistical analysis

Data were presented as mean values with their corresponding standard deviations. Statistical comparisons among groups were conducted using one-way analysis of variance (ANOVA) complemented by Tukey's post-hoc test, unless otherwise specified. A p-value of less than 0.05 was established as the threshold for statistical significance.

3. Result

3.1. Synthesis and physicochemical characterization of Pre-NPs and NO-NPs

The NO precursor (Pre-NPs) synthesized by mPEG, mercaptosuccinic acid (MS) and ethylene glycol (EG), formed NO donor (NO-NPs) through nitrite (Fig. 2A). ^{1}H NMR results were shown in Fig. 2B and C. In the ^{1}H NMR of Pre-NPs, the resonance absorption peak of –CH2- in mPEG is at 3.75 ppm, and the characteristic peak of –SH is at 2.3 ppm. In the HNMR of NO-NPs, the peak of –SH decreases, indicating that most of the –SH is nitrosated. Through the infrared spectrum, it can be observed that the peak of –SH (1600 cm^{-1}) decreases while the peak of –SNO (1600 and 764 cm^{-1}) appears (Fig. 2D). The thermogravimetric result indicates that Pre-NPs loses 2.01 % weight and NO-NPs loses 4.12 % weight before 200 °C (Fig. 2F). This difference is caused by the release of NO by NO-NPs. In the visible UV spectra, NO-NPs has a peak at 340 nm, which is the UV absorption peak of –SNO (Fig. 2E). According to transmission electron microscopy (TEM) images, both Pre-NPs and NO-NPs have relatively uniform micelle particle sizes. The average water and particle sizes are 126.81 nm and 68.10 nm, respectively (Fig. 2G). Due to the

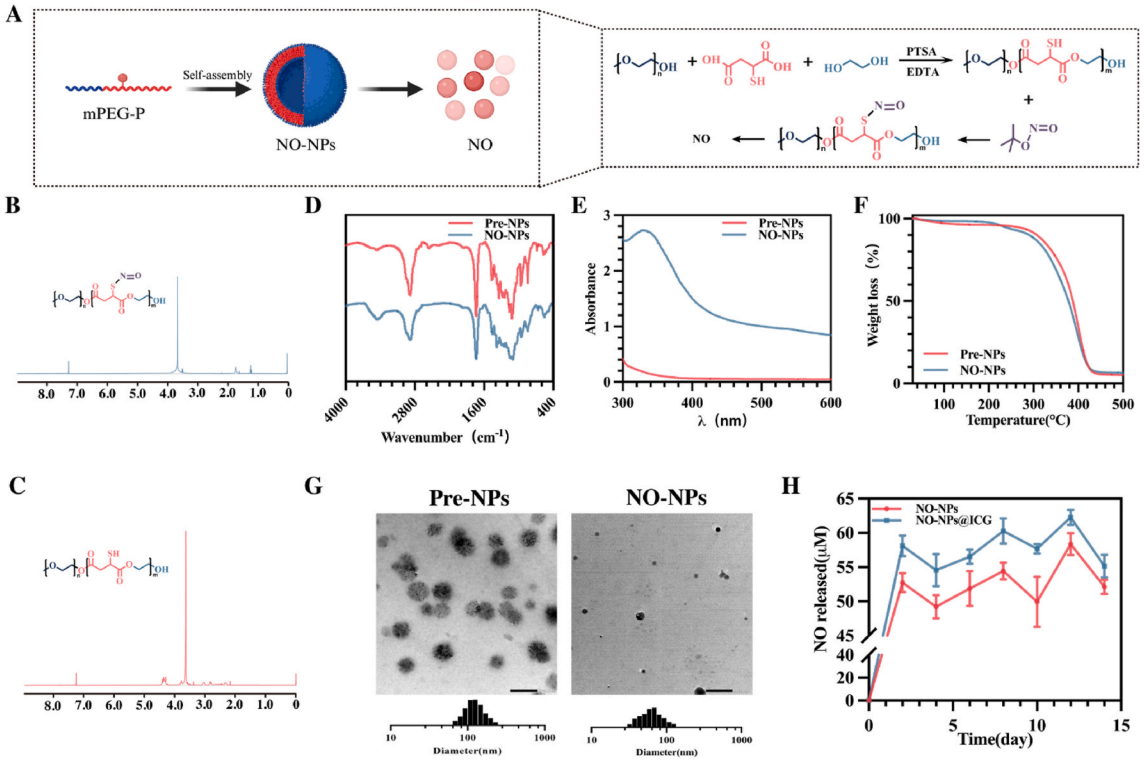

Fig. 2. Synthesis and physicochemical characterization of NO-NPs and Pre-NPs. (A) The synthesis mechanism of NO donors and Schematic diagram of NO-NPs ultrasonic self-assembly and NO release. (B, C) ^{1}H NMR spectra of Pre-NPs and NO-NPs. (D) FTIR of Pre-NPs and NO-NPs. (E) Ultraviolet–visible spectra of Pre-NPs and NO-NPs. (F) TA of Pre-NPs and NO-NPs. (G) TEM images of precursor-NPs and NO-NPs. (H) NO release curve of NO-NPs and NO-NPs@ICG within 2 weeks at room temperature.

ability of - SNO to generate NO under thermal action, ICG (a photothermal material) was added to nano micelles to promote the release of NO and stimulated by near-infrared light (808 nm, 1 W/cm^2) for 2 min daily. The NO content test results show that, the NO release from NO-NPs@ICG is higher than NO-NPs, and the NO concentration is 55 μM on the 14th day (Fig. 2H and S2). Subsequently, we examined the NO release behavior of NO-NPs under different pH values and temperatures. The results indicated that NO-NPs promoted NO release in both acidic and alkaline environments. Regarding temperature, the NO release rate was significantly higher at 40 °C compared to 25 °C and 10 °C (Fig. S3).

3.2. Synthesis and physicochemical characterization of mPEG-PA-PP

mPEG-PA-PP (temperature sensitive hydrogel) can be used as the carrier of NO-NPs @ICG and injected into the periosteal defect (Fig. 3A). ^{1}H NMR result of mPEG-PA-PP was shown in (Fig. S4). The scanning electron microscopy images of mPEG-PA-PP and NO-NPs@ICG/mPEG-PA-PP show that the addition of NO-NPs@ICG did not damage the porous structure of mPEG-PA-PP (Fig. 3B). The thermosensitive hydrogel is injectable, and the "WHU" in Fig. 3C is written by mPEG-PA-PP in the syringe. This hydrogel has a certain degradation performance, and its weight loss rate is 17.9 % on the 24th day (Fig. 3D). Based on rheological results, the gelation temperatures of mPEG-PA-PP and NO-NPs@ICG/mPEG-PA-PP are 30 °C and 29 °C, respectively (Fig. 3E). Adding NO-NPs@ICG does not have a significant impact on the temperature sensitivity of mPEG-PA-PP (Fig. 3F). The result of frequency-scan measurements (0.01–10 rad/s, 1 % strain) shows that the G' values of mPEG-PA-PP and NO-NPs@ICG/mPEG-PA-PP are positively correlated with frequency (Fig. 3G). The strain scanning results indicate that the addition of NO-NPs@ICG does not alter the storage modulus of mPEG-PA-PP (Fig. 3H).

3.3. In Vitro Evaluation of Cytocompatibility

To assess the release of NO from NO-NPs and NO-NPs@ICG during cell culture, we utilized the NO probe (DAF-FM DA) in conjunction with BMSCs cultivation. Our observations revealed that upon photothermal stimulation, the NO-NPs@ICG group exhibited the most pronounced fluorescence, indicating heightened NO release, whereas the NO-NPs group displayed a comparatively weaker response. Conversely, the Control and Pre-NPs groups showed negligible fluorescence levels (Fig. 4A and B).

Given the pivotal role of vascular endothelial cells and BMSCs viability and proliferation in bone repair processes, we conducted the in vitro cytotoxicity of NO-NPs and NO-NPs@ICG using BMSCs and HUVECs. Cell viability was monitored using the CCK-8 assay on days 1, 3, and 5 post-treatment with Pre-NPs, NO-NPs, and NO-NPs@ICG. Results from the CCK-8 assay demonstrated an increase in cell OD values over time across all groups, indicative of sustained cell activity and proliferation (Fig. 4C and E). Remarkably, comparable cell proliferation rates were observed across all groups on 1, 3 and 5 days. The favorable cell compatibility of the NPs was further confirmed through live/dead staining (Fig. S5), where BMSCs and HUVECs exhibited viability (green fluorescence) with minimal evidence of cell death (red fluorescence) after 5 days of co-culture. Additionally, cell apoptosis was assessed using Hoechst33258 staining, revealing that the majority of cells maintained

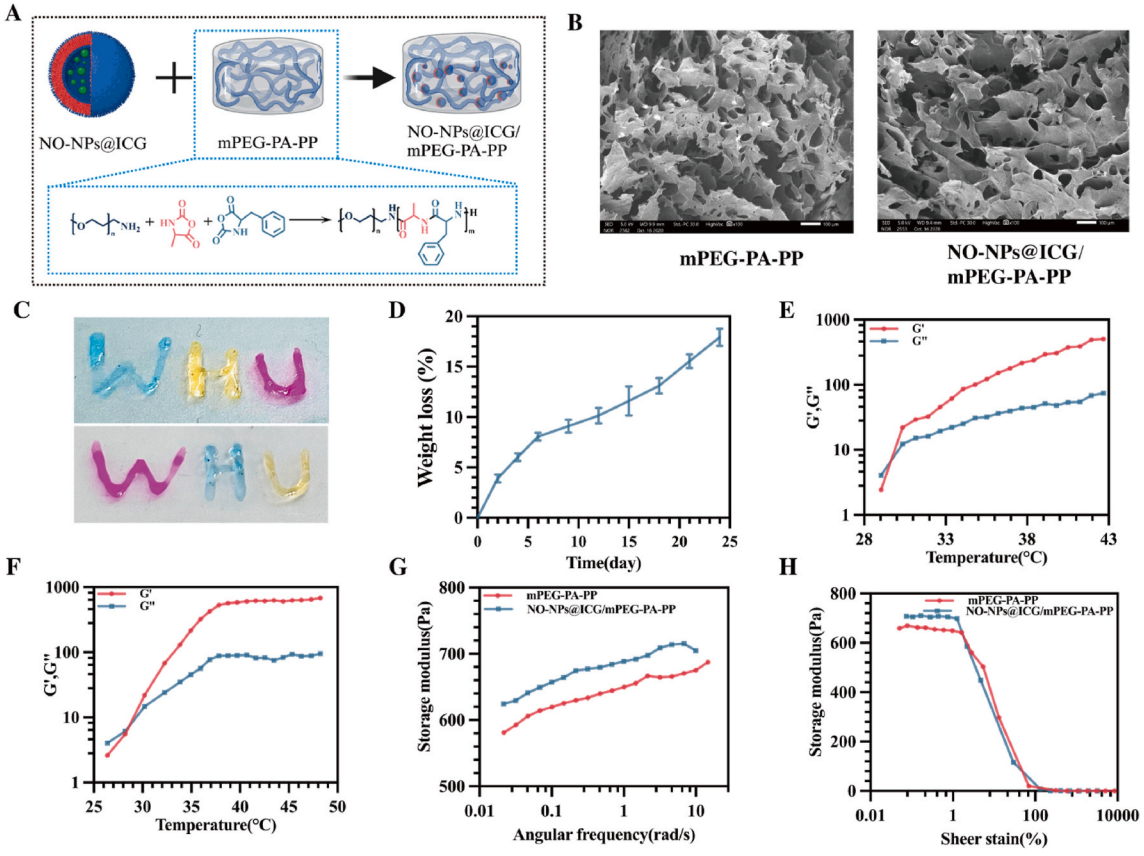

Fig. 3. Synthesis and physicochemical characterization of mPEG-PA-PP. (A) Schematic diagram of mPEG-PA-PP synthesis and loading of NO-NPs@ICG to construct an injectable NO sustained-release system. (B) SEM images of mPEG-PA-PP and NO-NPs@ICG/mPEG-PA-PP. (C) The injectability of mPEG-PA-PP hydrogels. (D) Weight loss rate of mPEG-PA-PP within 24 days of degradation. (E, F) Storage modulus G′ and loss modulus G″ of mPEG-PA-PP and NO-NPs@ICG/mPEG-PA-PP hydrogels (rotational rheological properties). (G) Frequency scanning measurement of mPEG-PA-PP and NO-NPs@ICG/mPEG-PA-PP hydrogel (0.01–10 rad/s; 1 % strain). (H) Storage modulus (G′) curve of mPEG-PA-PP and NO-NPs@ICG/mPEG-PA-PP hydrogel under rotational strain scanning (0.01–10000 % strain; 10 rad/s).

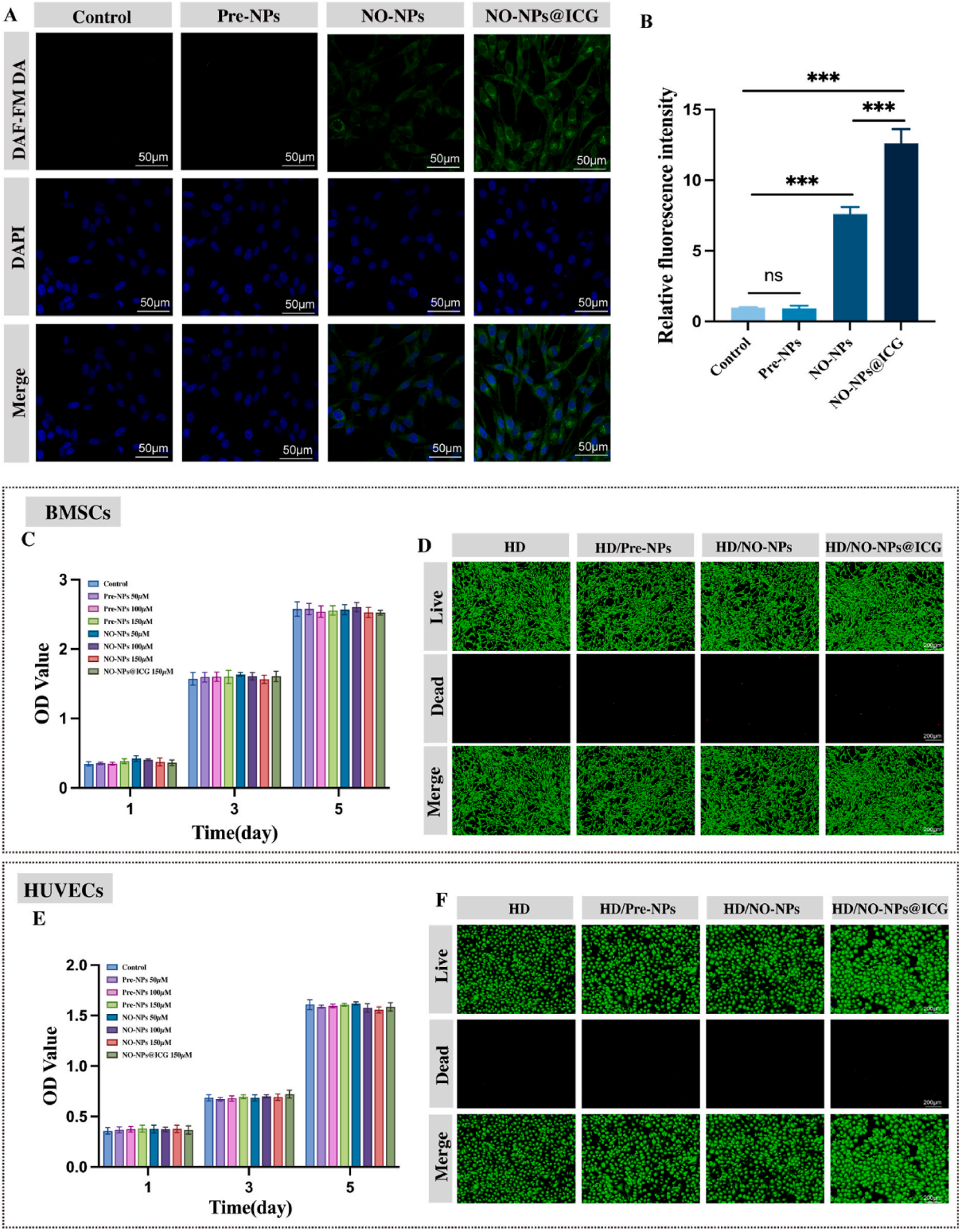

Fig. 4. In Vitro Evaluation of Cytocompatibility. (A) Fluorescence image of DAF-FM DA in BMSCs. (B) Quantification of fluorescence intensity of DAF-FM DA in BMSCs. (C) CCK-8 assay of BMSCs cultured with Different concentrations of NPs. (D) Live/dead staining of BMSCs cultured with HD for 5 days. (E) CCK-8 assay of HUVECs cultured with Different concentrations of NPs. (F) Live/dead staining of HUVECs cultured with HD for 5 days. Data are presented as the mean ± SD (n = 3). ***$p < 0.001$, ns = not significant.

intact nuclei (Fig. S5). Subsequently, the effect of mPEG-PA-PP hydrogel (HD) on BMSCs and HUVECs was evaluated in the transwell-based co-culture system. Hydrogels loaded with different NPs (100 μM) were placed in the upper chamber of the transwell, and cells were seeded into the bottom well of the transwell plate and co-cultured for 5 days. Live/dead staining affirmed the excellent biocompatibility of the hydrogel, with minimal evidence of cell death (Fig. 4D and F).

3.4. In vitro assessment of angiogenesis

The assessment of angiogenesis is a critical component in the reconstruction process of bone healing, with the regeneration of the vascular network being pivotal to the success of bone defect repair. The formation of tubular structures by endothelial cells serves as a key process and a vital indicator for evaluating vascular regeneration. To this end, we performed a tube formation assay to evaluate the effects of NO-NPs and NO-NPs@ICG on HUVECs in vitro endothelial tube formation. As depicted in Fig. 5A, after an 8-h incubation period, minimal

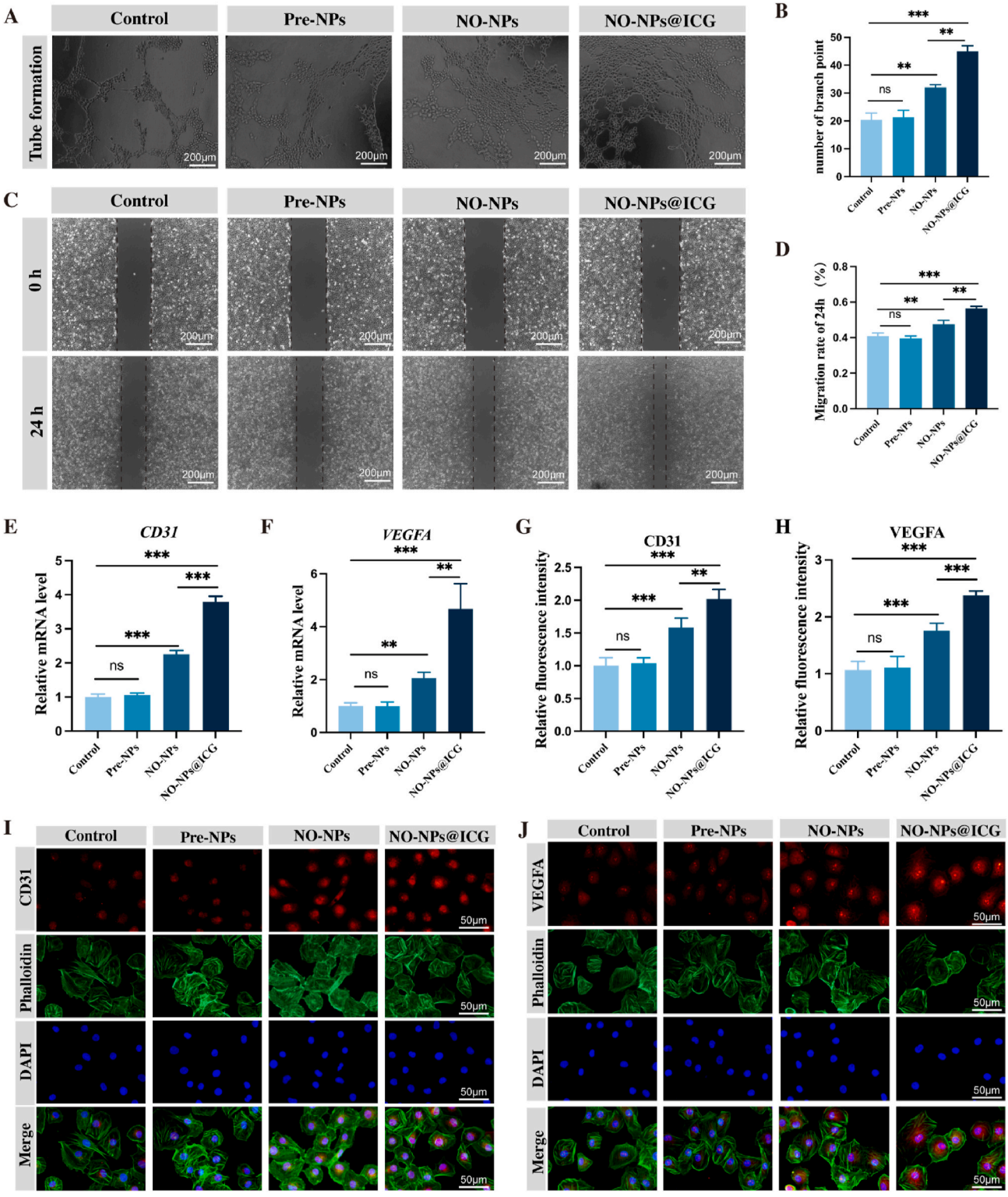

Fig. 5. In vitro assessment of angiogenesis. (A, B) The tube formation assay was conducted on HUVECs at 8 h, and the number of junctions assessed. (C) Cell scratch assay for HUVECs migration at 0, and 24 h. (D) Quantitative analysis of HUVECs migration rate at 24 h. (E, F) Relative mRNA expression of *CD31* and *VEGFA* in HUVECs, cultured with NPs at 5 days. (G, H) Quantification of fluorescence intensity of CD31 and VEGFA in HUVECs. (I, J) Immunofluorescence staining of CD31 and VEGFA in HUVECs, cultured with NPs at 5 days. Data are presented as the mean ± SD (n = 3). **p < 0.01, ***p < 0.001, ns = not significant.

tube formation was observed in the Control and Pre-NPs groups, suggesting a constrained capacity for vascular generation. In contrast, the NO-NPs and NO-NPs@ICG groups exhibited the formation of tubular frameworks, with the NO-NPs@ICG group showing more mature and complete structures and a higher density of cell connections (Fig. 5B). The migration capability of HUVECs was further assessed using a scratch assay, revealing that the NO-NPs and NO-NPs@ICG groups had significantly smaller wound closure areas and enhanced migration abilities at 24-h post-injury, with the NO-NPs@ICG group demonstrating a slightly superior migration rate (Fig. 5C and D).

VEGFA and CD31 are recognized markers for angiogenesis. To further investigate this, we conducted qRT-PCR analysis to assess the expression of these angiogenesis-related factors in HUVECs. The NO-NPs@ICG group exhibited the highest levels of *VEGFA* and *CD31* expression, attributed to the increased NO release facilitated by near infrared (NIR) irradiation. The NO-NPs group, which gradually released NO, also showed elevated *VEGFA* and *CD31* expression (Fig. 5E and F). The angiogenesis capability was further confirmed through immunofluorescent staining of CD31 and VEGFA. After 5 days of co-culture, both the NO-NPs and NO-NPs@ICG groups displayed a significant increase in CD31 protein expression, with the NO-NPs@ICG group showing the highest fluorescence signal, indicative of enhanced vascular formation (Fig. 5I). VEGFA expression followed a similar pattern, with the NO-NPs@ICG group leading and the NO-NPs group next (Fig. 5J). Quantitative analysis of fluorescence intensity further confirmed that the NO-NPs@ICG group had the most pronounced expression of vascular protein markers, suggesting a robust angiogenesis activity (Fig. 5G and H).

These results demonstrate that NO-NPs possess the ability to efficiently facilitate angiogenesis, and the NO release triggered by mild photothermal stimuli is shown to markedly enhance the rate of angiogenesis.

3.5. In vitro assessment of osteogenesis

As an indicator of early osteogenic differentiation, alkaline phosphatase (ALP) activity was qualitatively and quantitatively assessed in vitro. The NO-NPs@ICG group exhibited the most robust ALP activity, followed by the NO-NPs group, while the Control and Pre-NPs groups displayed weaker color intensity (Fig. 6A). This observation underscores the promotion of early osteogenic differentiation by NIR-induced NO-NPs@ICG. Consistent results were obtained through quantitative analysis of ALP activity (Fig. 6B). The deposition of calcium minerals, indicative of advanced osteogenic differentiation, was visualized using Alizarin Red S (AS) staining. As anticipated, the AS staining results mirrored those of ALP staining, with the NO-NPs@ICG group exhibiting the highest quantity of bone mineralization nodules, indicative of superior osteogenic potential. The NO-NPs group also displayed significantly more bone mineralization nodules compared to the Control and Pre-NPs groups (Fig. 6C). Quantitative analysis further corroborated these findings (Fig. 6D).

Given the integral roles of *Col1a1, Ocn, Bmp2,* and *Runx2* in bone extracellular matrix composition and osteogenesis regulation, we conducted additional analyses of their expression at both gene and protein levels. Western blot results demonstrated elevated expression levels of COL1a1, OCN, BMP2, and RUNX2 proteins in the NO-NPs and NO-NPs@ICG groups relative to the Control and Pre-NPs groups, indicating significant upregulation of osteogenic markers. Notably, the NO-NPs@ICG group exhibited the most pronounced enhancement in osteogenic markers expression, consistent with ALP and ARS assessments (Fig. 6I). Quantitative analysis of these markers was consistent with the Western blot results (Fig. S6). The mRNA expression levels of *Col1a1, Ocn, Bmp2,* and *Runx2* also mirrored these findings (Fig. 6E–H).

Immunofluorescence staining further confirmed the trend, revealing heightened secretion of osteogenic-related proteins by BMSCs in the NO-NPs and NO-NPs@ICG groups compared to the Control and Pre-NPs groups (Fig. 6L, M and S7). Strikingly, the NO-NPs@ICG group subjected to thermal stimulation following NIR irradiation exhibited the highest protein expression among all groups, signifying a substantial enhancement in osteogenic capacity. Quantitative analysis results reinforced this observation (Fig. 6J, K and S7).

Collectively, these findings underscore the significant stimulatory effect of the NO-NPs@ICG group on BMSCs osteogenic differentiation, suggesting its potential to promote bone healing through the upregulation of *Col1a1, Ocn, Bmp2,* and *Runx2* gene expression.

3.6. Activation of the SGC/PKG pathway in vitro and in vivo

To assess the mRNA expression levels of *SGC* and *PKG*, qRT-PCR analyses were conducted. Results revealed elevated mRNA levels of *Sgc* and *Pkg* in BMSCs treated with NO-NPs compared to the Control and Pre-NPs groups. Furthermore, the NO-NPs@ICG group, following NIR irradiation, exhibited heightened NO release, leading to a significant increase in *Sgc* and *Pkg* mRNA levels (Fig. 7A). The expression trends of *SGC* and *PKG* in HUVECs were consistent with those observed in BMSCs (Fig. 7D). Subsequent evaluation of protein expression via Western blotting corroborated these findings, with the NO-NPs@ICG group displaying the highest expression levels, consistent with the mRNA expression trend (Fig. 7C and F). Quantitative analysis of protein expression further supported these observations (Fig. 7B and E).

To validate the expression levels of the SGC/PKG signaling pathway in vivo, immunofluorescent staining of SGC and PKG was performed on histological sections of rat calvarial defect tissues. Results mirrored those obtained in vitro, with the HD/NO-NPs@ICG and HD/NO-NPs groups exhibiting stronger positive staining compared to the HD and HD/Pre-NPs groups. Notably, the HD/NO-NPs@ICG group displayed the highest positive fluorescence intensity (Fig. 7G).

To elucidate the underlying mechanisms, we employed the PKG inhibitor KT5823. Initially, using the CCK-8 assay, we evaluated the impact of KT5823 on BMSCs and HUVECs. The results indicated that KT5823, at various concentrations, did not affect the viability or proliferative capacity of BMSCs and HUVECs (Figs. S8A and B). Subsequent RT-PCR analysis revealed that KT5823 significantly downregulated the mRNA expression levels of *PKG* (Fig. S8C). Furthermore, Western blotting was employed to assess the effects of KT5823 on osteogenic and angiogenic capabilities. The findings demonstrated that, compared to the Control group, NO-NP@ICG enhanced the expression of osteogenic-related proteins in BMSCs. However, KT5823 attenuated the osteogenic promotion effect of NO-NP@ICG (Figs. S8D and E). Similarly, in HUVECs, KT5823 also reduced the expression levels of VEGFA (Figs. S8F and G).

In summary, NO-NPs activate the SGC/PKG pathway through NO release, promoting osteogenesis and angiogenesis in vitro. The application of NO-NPs@ICG, coupled with photothermal effects, enhances NO release, consequently activating the SCG/PKG pathway earlier and achieving elevated expression levels of osteogenic and angiogenic markers.

3.7. Evaluation of bone repair in bone defects

Based on the preceding results, our formulated NO-NPs@ICG demonstrate promising osteogenic and angiogenic capabilities, indicating significant potential in expediting bone tissue repair. However, it remains imperative to ascertain whether these advantageous effects can be translated into in vivo settings. To address this, a critical-sized rat calvarial defect model ($\Phi = 5$ mm) was established to further evaluate the impact of NO-NPs@ICG on bone repair in vivo. After a six-week post-surgery period, the bone repair process was comprehensively assessed from both macroscopic and microscopic perspectives employing micro-computed tomography (micro-CT) and histological analysis. The 3D reconstruction images of rat calvarial defect repair unveiled that the HD/NO-NPs and HD/NO-NPs@ICG groups exhibited substantial bone tissue regeneration, not only growing inward along the edges of the

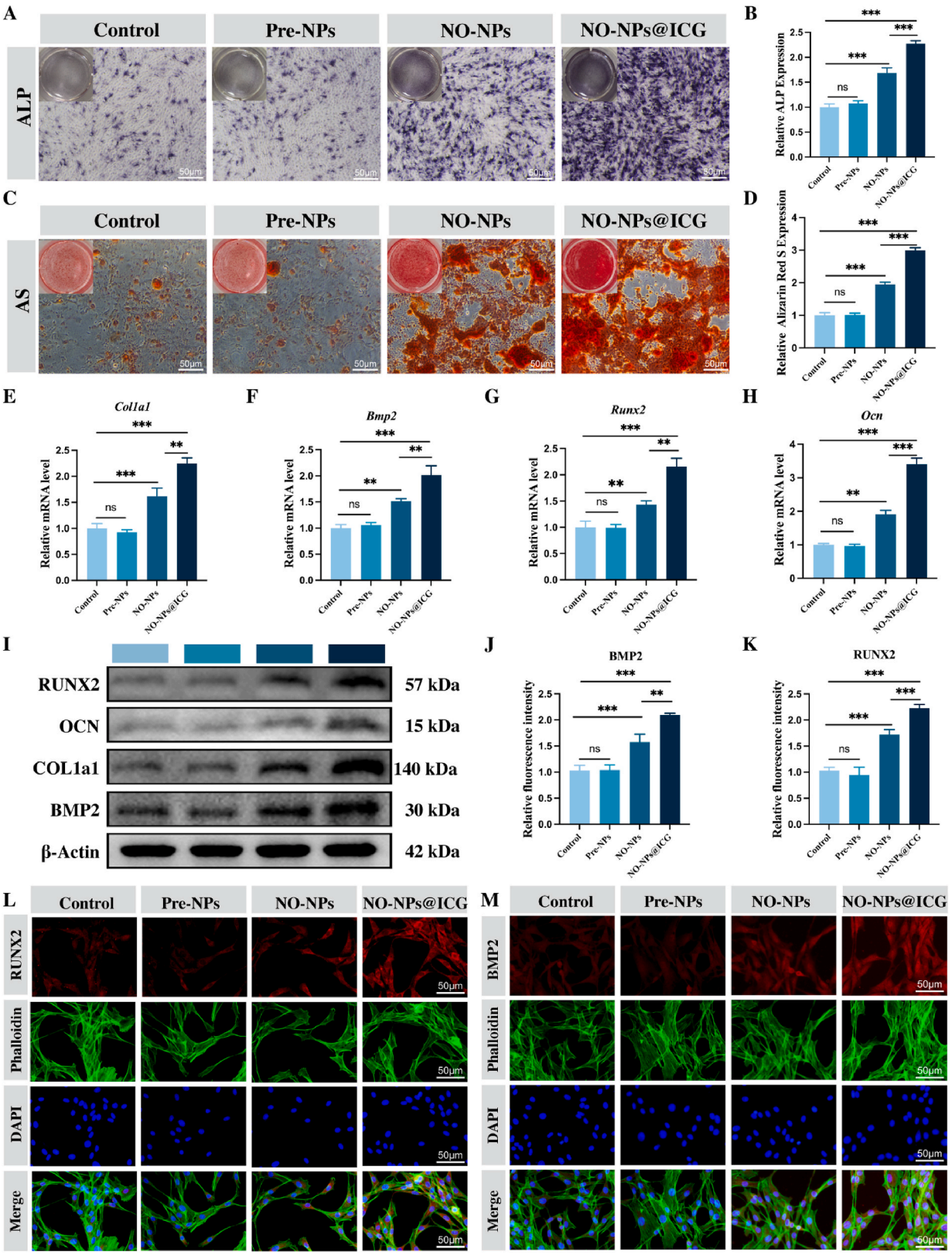

Fig. 6. In vitro assessment of osteogenesis. (A, B) Staining of ALP at 7 days and quantitative analysis of ALP activity. (C, D) An analysis of AS at 21 days and quantitative analysis of alizarin red. (E–H) Relative mRNA expression of *Col1a1, Ocn, Bmp2,* and *Runx2* in BMSCs, cultured in osteogenic induction medium at 3 days. (I) Western blot analysis of COL1a1, BMP2, OCN and RUNX2 protein expression in BMSCs cultured in osteogenic induction medium at 3 days. (J, K) Quantification of fluorescence intensity of RUNX2 and BMP2 in BMSCs. (L, M) Immunofluorescence staining of RUNX2 and BMP2 in BMSCs. Data are presented as the mean ± SD (n = 3). $^{**}p < 0.01$, $^{***}p < 0.001$, ns = not significant. (For interpretation of the references to color in this figure legend, the reader is referred to the Web version of this article.)

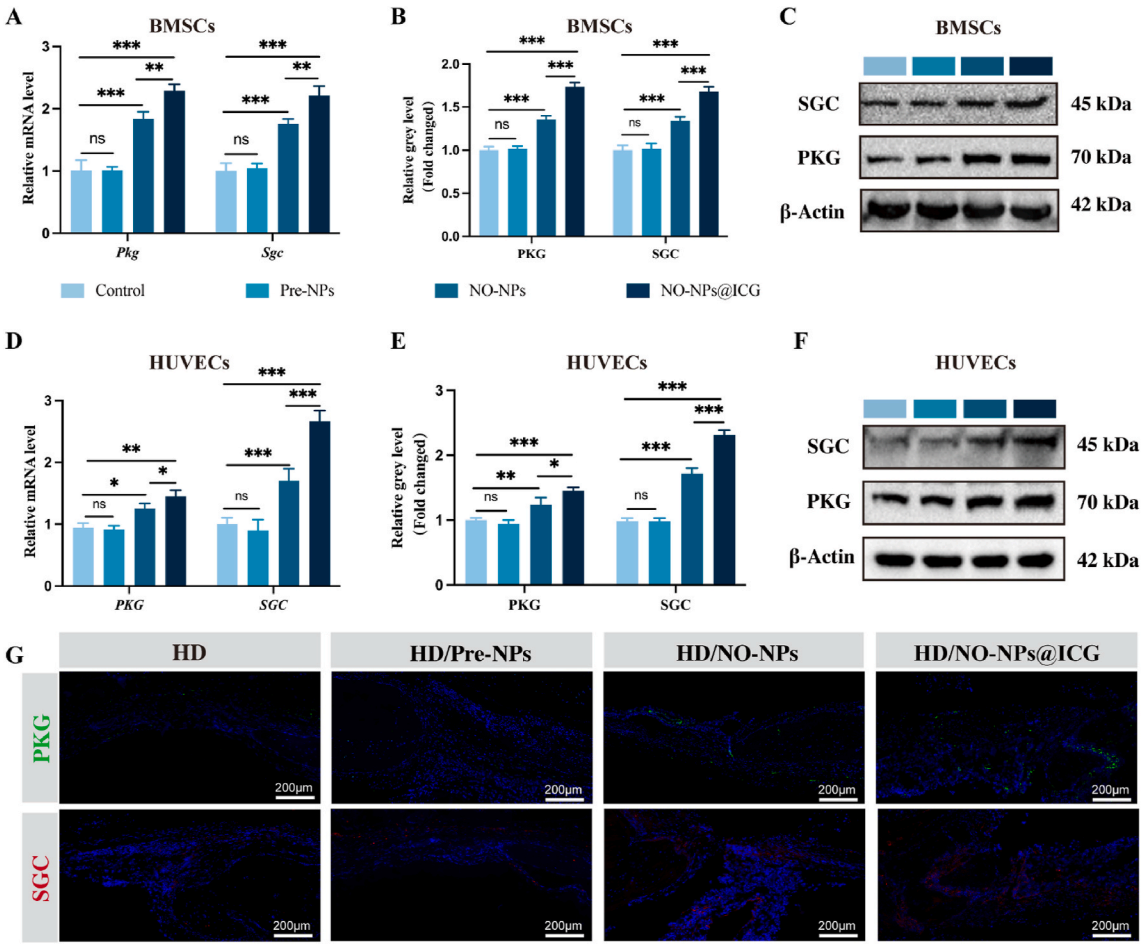

Fig. 7. Activation of SGC/PKG signal pathway. (A) Relative mRNA expression of *Pkg* and *Sgc* in BMSCs. (B, C) Western blot analysis and quantification of PKG and SGC protein expression in BMSCs. (D) Relative mRNA expression of *PKG* and *SGC* in HUVECs. (E, F) Western blot analysis and quantification of PKG and SGC protein expression in HUVECs. (G) Immunofluorescence staining of PKG and SGC of defect areas at 6 weeks. Data are presented as the mean ± SD (n = 3). *p < 0.05, **p < 0.01, ***p < 0.001, ns = not significant.

defect but also filling spaces unconnected to the defect edges. In contrast, the HD and HD/Pre-NPs groups displayed evident defects with no significant bone formation at the edges, indicative of limited self-repair capacity (Fig. 8A). Quantitative analysis of bone tissue volume/total tissue volume (BV/TV) further corroborated these observations, with the HD/NO-NPs@ICG group achieving the highest BV/TV (38.22 ± 1.51 %) at six weeks, surpassing the HD/NO-NPs group (31.14 ± 1.91 %), HD/Pre-NPs group (14.02 ± 1.50 %), and HA group (14.56 ± 0.76 %) (Fig. 8B). Additionally, key indicators for assessing bone regeneration efficacy include Trabecular Thickness (Tb.Th, 0.38 ± 0.015 mm), Trabecular Number (Tb.N, 0.445 ± 0.025 mm^{-1}), and Bone Mineral Density (BMD, 0.28 ± 0.016 g/cm^3). The HD/NO-NPs@ICG group exhibited the highest values, followed by the HD/NO-NPs group, with a trend consistent with BV/TV (Fig. S9). This enhanced bone regeneration in the HD/NO-NPs@ICG group may be attributed to the responsive characteristics of NIR and ICG, where photothermal effects rapidly augment NO release, thereby facilitating early vascular formation during the bone healing process and ultimately accelerating bone mineralization.

Subsequently, the histological structure of the regenerated new bone at the defect site was confirmed using H&E and Masson staining, which further validated the microscopic details observed in micro-CT images. Evidently, histological examination revealed extensive fibrous tissue growth into the defect in the surrounding areas of the HD and HD/Pre-NPs groups, hindering bone regeneration and resulting in nonunion. Instead, the HD/NO-NPs and HD/NO-NPs@ICG groups exhibited evident new bone tissue at the defect edges, emphasizing successful bone regeneration (Fig. 8C). Masson staining highlighted regular lamellar bone in the HD/NO-NPs and HD/NO-NPs@ICG groups, while the HD and HD/Pre-NPs groups displayed more pronounced blue collagen fibers with less bone formation (Fig. 8D).

3.8. Analysis of vascularization and osteogenesis in bone defects

To further validate the in vivo biomineralization and angiogenic capabilities, immunohistochemical staining for CD31, VEGFA, RUNX2, and OCN was conducted six weeks post-implantation. As depicted in Fig. 9A, the HD/NO-NPs@ICG group exhibited a notable abundance of CD31-positive circular or elliptical new blood vessels, followed by the HD/NO-NPs group, while the HD and HD/Pre-NPs groups displayed minimal CD31 staining. Similarly, the expression of VEGFA, RUNX2, and OCN proteins was markedly higher in the HD/NO-NPs and HD/NO-NPs@ICG groups compared to the HD and HD/Pre-NPs groups, with the HD/NO-NPs@ICG group demonstrating the strongest positive staining for VEGFA, RUNX2, and OCN proteins. Additionally, protein blotting of tissue proteins extracted from the defect area revealed the highest protein expression in the HD/NO-NPs@ICG group, followed by the HD/NO-NPs group, whereas the expression levels in the HD and HD/Pre-NPs groups were notably lower than the former two groups (Fig. 9B). Quantitative analysis results aligned with our previous findings (Fig. 9C–G).

Moreover, compared to non-operated normal rats, no significant

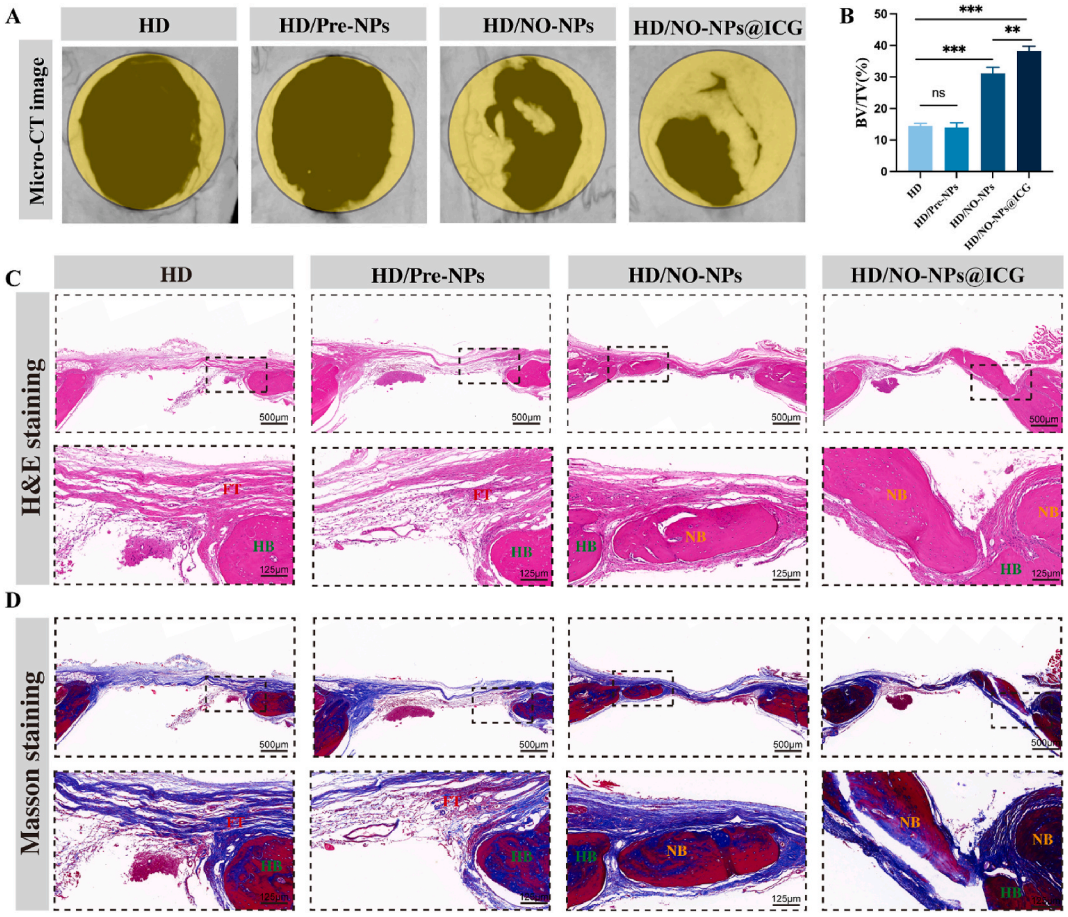

Fig. 8. Evaluation of Bone Repair in bone defects. (A) 6 weeks 3D reconstruction of defect areas. (B) Quantification of BV/TV in the defect area. (C) H&E staining of the bone defect at 6 weeks. (D) Masson staining of the bone defect at 6 weeks. HB indicated as host bone, NB as new bone, and FT as fibrous tissue. Data are presented as the mean ± SD (n = 3). **p < 0.01, ***p < 0.001, ns = not significant.

pathological changes were observed in the heart, lungs, liver, spleen, kidneys, or other major organs in all experimental groups, indicating good biocompatibility of the hydrogel and nanoparticles in vivo (Fig. S10).

4. Discussion

Bone defect repair represents a multifaceted and protracted process orchestrated by various cellular players, including mesenchymal stem cells, endothelial cells, and macrophages [31–33]. Among these, angiogenesis emerges as a pivotal aspect, crucial for furnishing bone tissue with indispensable minerals, growth factors, and orchestrating calcium salt deposition. Additionally, angiogenesis assumes a regulatory role in cell growth, differentiation, and regeneration through paracrine signaling pathways [34–36]. In the context of biomaterial-induced bone tissue regeneration, the timely establishment of a vascular network assumes paramount importance for ensuring effective bone repair [37]. Indeed, insufficient blood supply during bone tissue regeneration poses a significant hurdle to bone defect repair and subsequent tissue reconstruction. Consequently, addressing strategies aimed at promoting the rapid vascularization of bone biomaterials post-grafting, along with the establishment of a robust vascular network to support new bone formation and facilitate nutrient supply, represents a critical challenge currently confronting the field.

VEGFA stands as a pivotal growth factor governing both vascular development and angiogenesis, while also exerting significant influence on bone development [38]. Research indicates that VEGFA not only facilitates osteogenesis in conjunction with vascular regeneration but also contributes to bone progenitor cell development and maturation. Particularly under conditions of inflammation and hypoxia, osteoblasts stimulate VEGFA release via the HIF-1α pathway, thereby activating vascular endothelial cells and enhancing vascular permeability. This process not only ensures the provision of crucial nutrients, oxygen, and minerals to bone progenitor cells but also fosters their development and maturation [39].Conversely, mature osteoblasts reciprocally secrete angiogenic factors such as VEGFA, thus further bolstering angiogenesis. NO, as an endogenous vascular modulator, plays a significant role in regulating vascular function and regeneration processes. Continuous NO production triggers SGC activation, subsequently initiating the cGMP signaling pathway and culminating in elevated expression of the angiogenic factor VEGFA. In our study, we introduce a system designed to expedite NO release via the photothermal effect. This mechanism facilitates early elevation of VEGFA levels, promotes endothelial cell maturation, and fosters angiogenesis at the defect site, thereby supplying the essential nutrients requisite for bone repair.

Endogenous NO production plays a vital role in maintaining skeletal homeostasis. Produced in vivo by nitric oxide synthase (NOS), endogenous NO contributes significantly to the proliferation and differentiation of osteoblasts. Research indicates that NOS expression is increased during the bone healing process in both humans and animals, while the application of a non-specific NOS inhibitor can suppress fracture healing [40]. Additionally, NO plays a critical role in osteoclast activity. A reduction in endogenous NO levels can activate osteoclasts, increasing bone resorption, whereas high concentrations of NO inhibit the expression of bone resorption-related cytokines [41].Studies targeting endothelial NOS (eNOS) in mice through knockout experiments have

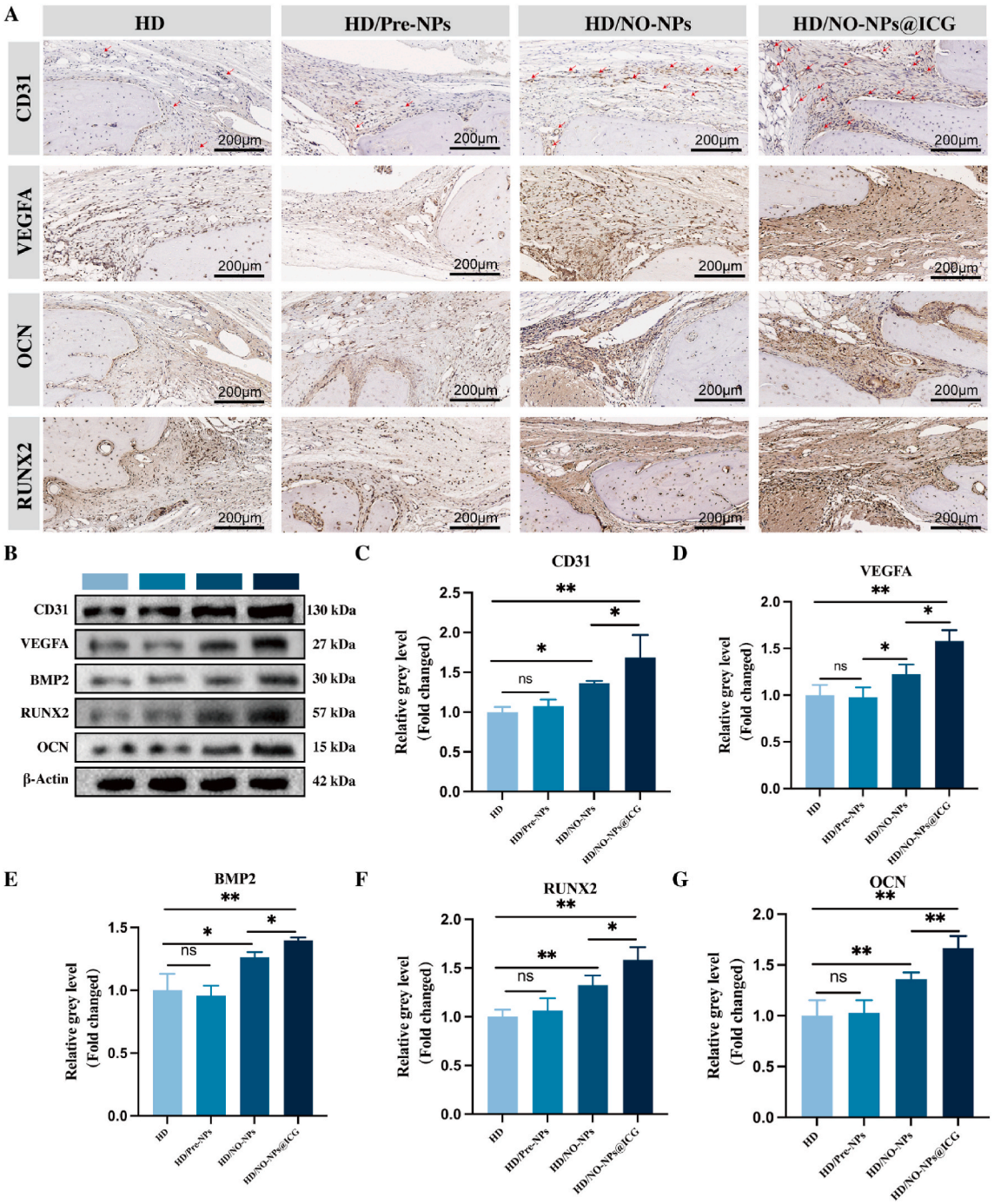

Fig. 9. Vascularization and osteogenesis in bone defects. (A) Immunohistochemical staining of CD31, VEGFA, OCN, and RUNX2 for the bone defect at 6 weeks. Red arrows as blood vessel. (B) Western blot analysis of osteogenic and angiogenesis-related genes protein expression. (C–G) Quantification of osteogenic and angiogenesis-related genes protein expression. Data are presented as the mean ± SD (n = 3). *p < 0.05, **p < 0.01, ns = not significant. (For interpretation of the references to color in this figure legend, the reader is referred to the Web version of this article.)

demonstrated inhibited proliferation and reduced activity of osteoblasts cultured from their tissues [42]. However, upon incubation with the NO donor SNAP, these cells exhibited a notable improvement in cell number and reactive alkaline phosphatase activity, underscoring the potential of exogenous NO in promoting bone growth and repair [42]. Moreover, exogenous NO has been shown to promote osteoblast proliferation, preserve bone mass, and mitigate postmenopausal-induced osteoporosis. Despite the promising effects of NO on bone health, research on its application in bone defect repair remains relatively limited. In our study, the NO release system designed exhibited the ability to promote bone formation and mineralization both ex vivo and in vivo by continuously releasing NO. This led to increased expression of cGMP and upregulation of osteogenesis-related factors such as RUNX2, ALP and OCN. These findings underscore the potential of NO-based strategies in enhancing bone repair and regeneration.

The downstream effector proteins of cGMP in bone are primarily PKG1α, PKG1β, and PKG2. These isoforms are expressed simultaneously in bone metabolism and fulfill different functions. PKG1β is the main PKG isoform in human osteoclasts, promoting the dissociation of the IP3R1-IRAG complex and ensuring osteoclast functional stability [43].

PKG2 acts in osteoblasts by activating ERK and Akt, which directly phosphorylate and regulate the interaction between pro-apoptotic protein BAD and anti-apoptotic protein Bcl-2, thereby providing anti-apoptotic effects [24]. Additionally, Akt inhibits glycogen synthase kinase-3β expression, causing β-catenin nuclear translocation and Wnt pathway activation, which supports bone repair [24,44]. PKG1α promotes survival signaling through the direct phosphorylation of BAD [43]. Recent research also indicates that the positive effects of NO on bone synthesis may involve the enhancement of glycolysis in osteoblasts. Impaired NO sources lead to reduced mRNA levels of glycolysis-related genes (*Slc2a1, Pfkfb3, Ldha*), which decreases osteoblast differentiation capability [45]. While the positive role of cGMP/PKG in osteogenesis has been documented, further investigation is required to understand their additional roles in bone remodeling.

pH variations in the microenvironment are critical in regulating bone remodeling by influencing the physiological functions of cells such as osteoblasts and BMSCs [46]. Research indicates that osteoblast activity and proliferation are significantly reduced in acidic environments, whereas they are enhanced in weakly alkaline pH values ranging from 7.0 to 7.6, leading to increased bone mineralization capacity [47]. During the early stages of bone defects, the pH decreases from 7.4 to an acidic 6.8 due to inflammation, while in the mid-stages, as the repair process advances, the pH shifts towards alkaline conditions [48]. In this study, the nanoparticles demonstrated adaptability to the mildly acidic environment of early bone defects, effectively accelerating the release of NO and promoting the bone reconstruction process. Additionally, the body temperature of rats at 38 °C, compared to the ambient temperature of 25 °C, further enhanced the release of NO. The mPEG-PP-PA, composed of amide bonds, exhibited good stability at pH 6–8 and body temperature, providing optimal attachment points for the nanoparticles.

Scaffolds emerge as critical components in the management of substantial bone defects, serving as conduits for tissue growth during the bone repair continuum [49–52]. Injectable biomaterials, notably injectable hydrogels necessitating minimally invasive implantation, have exhibited considerable promise in ameliorating irregular critical-sized bone defects [53–56]. Characterized by their porous structure and extensive surface area, hydrogels mimic the extracellular matrix, furnishing numerous anchoring sites for cells while concurrently occupying the bone defect to impede premature fibrous connective tissue invasion. This, in turn, facilitates the recruitment of a plethora of mesenchymal stem cells from the bone marrow cavity post-defect [57–59]. In this study, NO-releasing nanoparticles were incorporated into a thermosensitive hydrogel (mPEG-PP-PA), which solidifies upon implantation due to elevated body temperature, thereby filling the bone defect site.

The swift release and accumulation of NO have the potential to elicit inflammatory responses and cellular apoptosis [60–62]. To mitigate this, the NO donor formulated in this study comprises hydrophilic and hydrophobic segments, enabling nanoparticle formation via ultrasound-induced self-assembly in aqueous environments, thereby tempering the NO release kinetics. Furthermore, the combined photothermal impact of a minute quantity of ICG and mild near-infrared light stimulation elicited an upsurge in NO release, with no discernible induction of cellular apoptosis observed following 5 days of co-culture.

Nonetheless, our study possesses certain limitations. Firstly, we did not juxtapose our NO release system with commercially available NO donors. Moreover, the pivotal role of macrophages in the bone defect repair cascade, along with the regulatory influence of NO on macrophages during bone repair, remains nebulous and warrants further investigation [19]. In summation, armed with a deeper comprehension of the biological underpinnings of NO and the continual evolution of material science, one anticipates the emergence of innovative NO-releasing biomaterials poised to facilitate convenient, enduring, and precise applications within the realms of tissue engineering and regenerative medicine.

5. Conclusion

In summary, this study introduces a novel therapeutic strategy for addressing critical bone defects through the development of a photothermally-enhance NO release system. ICG is encapsulated within NO nanoparticles and incorporated into a thermosensitive injectable hydrogel, facilitating prompt NO release upon NIR activation. This orchestrated release triggers the SCG/PKG signaling pathway, orchestrating synergistic effects of osteogenesis and angiogenesis, thereby expediting bone defect repair. In vitro investigations underscore the system's commendable biocompatibility, osteogenic, and angiogenic potential under appropriate NIR irradiation. Subsequent in vivo assessments validate that NIR-assisted GA/NO-NPs@ICG elicits notable neovascularization and osteogenic responses during the healing trajectory of critical bone defects in a rat model. In conclusion, this research introduces a pioneering therapeutic avenue for bone regeneration by efficaciously delivering NO release to stimulate early vascularization, thus heralding a transformative approach to mitigating the challenge posed by bone defects.

Funding

This study was supported by the National Natural Science Foundation of China (NSFC) (No.81972066).

Ethics approval and consent to participate

All animal experiment procedures have been approved by the experimental animal welfare ethics committee of Zhongnan Hospital of Wuhan University (Approval No. ZN20230864).

Consent for publication

All authors agree to be published.

CRediT authorship contribution statement

Yannan Cheng: Writing – review & editing, Writing – original draft, Methodology, Investigation, Formal analysis, Data curation, Conceptualization. **Yuanfang Huo:** Writing – review & editing, Writing – original draft, Project administration, Methodology, Investigation, Formal analysis, Data curation, Conceptualization. **Yongle Yu:** Writing – review & editing, Writing – original draft, Project administration, Formal analysis, Data curation, Conceptualization. **Ping Duan:** Methodology, Data curation, Conceptualization. **Xianzhen Dong:** Methodology, Data curation, Conceptualization. **Zirui Yu:** Visualization, Validation, Software, Methodology, Investigation, Conceptualization. **Qiang Cheng:** Methodology, Data curation, Conceptualization. **Honglian Dai:** Writing – review & editing, Supervision, Project administration, Funding acquisition, Conceptualization. **Zhenyu Pan:** Writing – review & editing, Supervision, Project administration, Funding acquisition, Conceptualization.

Declaration of competing interest

The authors declare that they have no known competing financial interests or personal relationships that could have appeared to influence the work reported in this paper.

Data availability

Data will be made available on request.

Acknowledgements

We thank BioRender.com for providing the drawing platform. This

work was supported by grants from the National Natural Science Foundation of China (52372272) and the Key Basic Research Program of Shenzhen (JCYJ20200109150218836).

Abbreviations

NO	Nitric Oxide
NPs	Nanoparticles
NIR	Near infrared
ICG	Indocyanine green
BMSCs	Bone marrow mesenchymal stem cells
HUVECs	Human umbilical vein endothelial cells
SGC	Soluble guanylate cyclase
cGMP	Cyclic guanosine monophosphate
BV/TV	Bone tissue volume/total tissue volume
BMD	Bone Mineral Density
Tb.Th	Trabecular Thickness
Tb.N	Trabecular Number
PKG	Protein kinase G
CD31	Platelet endothelial cell adhesion molecule-1
VEGFA	Vascular endothelial growth factor
RUNX2	Runt-related transcription factor-2
COL1a1	Collagen type I alpha 1
OCN	Osteocalcin
BMP2	Bone morphogenetic protein 2
ALP	Alkaline phosphatase
AS	Alizarin red S

Appendix A. Supplementary data

Supplementary data to this article can be found online at https://doi.org/10.1016/j.mtbio.2024.101180.

References

[1] X. Huang, Y. Lou, Y. Duan, H. Liu, J. Tian, Y. Shen, X. Wei, Biomaterial scaffolds in maxillofacial bone tissue engineering: a review of recent advances, Bioact Mater 33 (2024) 129–156.
[2] A. Salhotra, H.N. Shah, B. Levi, M.T. Longaker, Mechanisms of bone development and repair, Nat. Rev. Mol. Cell Biol. 21 (11) (2020) 696–711.
[3] A. Nauth, E. Schemitsch, B. Norris, Z. Nollin, J.T. Watson, Critical-size bone defects: is there a consensus for diagnosis and treatment? J. Orthop. Trauma 32 (Suppl 1) (2018) S7–s11.
[4] E. Gómez-Barrena, C. Ehrnthaller, Long bone uninfected non-union: grafting techniques, EFORT open reviews 9 (5) (2024) 329–338.
[5] J. Huang, Q. Han, M. Cai, J. Zhu, L. Li, L. Yu, Z. Wang, G. Fan, Y. Zhu, J. Lu, G. Zhou, Effect of angiogenesis in bone tissue engineering, Ann. Biomed. Eng. 50 (8) (2022) 898–913.
[6] X. Hu, J. Chen, S. Yang, Z. Zhang, H. Wu, J. He, L. Qin, J. Cao, C. Xiong, K. Li, X. Liu, Z. Qian, 3D printed multifunctional biomimetic bone scaffold combined with TP-Mg nanoparticles for the infectious bone defects repair, Small (2024) e2403681.
[7] J.K. Lee, D.S. Kim, S.Y. Park, S.W. Baek, J.W. Jung, T.H. Kim, D.K. Han, Nitric oxide-releasing bioinspired scaffold for exquisite regeneration of osteoporotic bone via regulation of homeostasis, Adv. Sci. 10 (6) (2023) e2205336.
[8] P.M. Sivakumar, A.A. Yetisgin, S.B. Sahin, E. Demir, S. Cetinel, Bone tissue engineering: anionic polysaccharides as promising scaffolds, Carbohydr. Polym. 283 (2022) 119142.
[9] T.M. Koushik, C.M. Miller, E. Antunes, Bone tissue engineering scaffolds: function of multi-material hierarchically structured scaffolds, Adv. Healthcare Mater. 12 (9) (2023) e2202766.
[10] T. Xu, Y. Yang, D. Suo, H.P. Bei, X. Xu, X. Zhao, Electrosprayed regeneration-enhancer-element microspheres power osteogenesis and angiogenesis coupling, Small 18 (36) (2022) e2200314.
[11] Y. Yang, T. Xu, Q. Zhang, Y. Piao, H.P. Bei, X. Zhao, Biomimetic, stiff, and adhesive periosteum with osteogenic-angiogenic coupling effect for bone regeneration, Small 17 (14) (2021) e2006598.
[12] J. Tuckermann, R.H. Adams, The endothelium-bone axis in development, homeostasis and bone and joint disease, Nat. Rev. Rheumatol. 17 (10) (2021) 608–620.
[13] F. Simunovic, G. Finkenzeller, Vascularization strategies in bone tissue engineering, Cells 10 (7) (2021).
[14] Y. Li, B. Yoon, A. Dey, V.Q. Nguyen, J.H. Park, Recent progress in nitric oxide-generating nanomedicine for cancer therapy, J. Contr. Release 352 (2022) 179–198.
[15] J. Jimenez, P. Dubey, B. Carter, J.M. Koomen, J. Markowitz, A metabolic perspective on nitric oxide function in melanoma, Biochim. Biophys. Acta Rev. Canc 1879 (1) (2024) 189038.
[16] L.B. Vong, T.Q. Bui, T. Tomita, H. Sakamoto, Y. Hiramatsu, Y. Nagasaki, Novel angiogenesis therapeutics by redox injectable hydrogel - regulation of local nitric oxide generation for effective cardiovascular therapy, Biomaterials 167 (2018) 143–152.
[17] J. Chen, D. Sheng, T. Ying, H. Zhao, J. Zhang, Y. Li, H. Xu, S. Chen, MOFs-based nitric oxide therapy for tendon regeneration, Nano-Micro Lett. 13 (1) (2020) 23.
[18] Y.C. Sung, P.R. Jin, L.A. Chu, F.F. Hsu, M.R. Wang, C.C. Chang, S.J. Chiou, J.T. Qiu, D.Y. Gao, C.C. Lin, Y.S. Chen, Y.C. Hsu, J. Wang, F.N. Wang, P.L. Yu, A.S. Chiang, A.Y. Wu, J.J. Ko, C.P. Lai, T.T. Lu, Y. Chen, Delivery of nitric oxide with a nanocarrier promotes tumour vessel normalization and potentiates anti-cancer therapies, Nat. Nanotechnol. 14 (12) (2019) 1160–1169.
[19] J. Ye, J. Jiang, Z. Zhou, Z. Weng, Y. Xu, L. Liu, W. Zhang, Y. Yang, J. Luo, X. Wang, Near-infrared light and upconversion nanoparticle defined nitric oxide-based osteoporosis targeting therapy, ACS Nano 15 (8) (2021) 13692–13702.
[20] Y.J. Lin, C.C. Chen, N.W. Chi, T. Nguyen, H.Y. Lu, D. Nguyen, P.L. Lai, H.W. Sung, In situ self-assembling micellar depots that can actively trap and passively release NO with long-lasting activity to reverse osteoporosis, Adv. Mater. 30 (22) (2018) e1705605.
[21] F. Wang, K. Qin, K. Wang, H. Wang, Q. Liu, M. Qian, S. Chen, Y. Sun, J. Hou, Y. Wei, Y. Hu, Z. Li, Q. Xu, Q. Zhao, Nitric oxide improves regeneration and prevents calcification in bio-hybrid vascular grafts via regulation of vascular stem/progenitor cells, Cell Rep. 39 (12) (2022) 110981.
[22] F. Triposkiadis, A. Xanthopoulos, J. Skoularigis, R.C. Starling, Therapeutic augmentation of NO-sGC-cGMP signalling: lessons learned from pulmonary arterial hypertension and heart failure, Heart Fail. Rev. 27 (6) (2022) 1991–2003.
[23] S.M. Kim, T. Yuen, J. Iqbal, M.R. Rubin, M. Zaidi, The NO-cGMP-PKG pathway in skeletal remodeling, Ann. N. Y. Acad. Sci. 1487 (1) (2021) 21–30.
[24] N. Marathe, H. Rangaswami, S. Zhuang, G.R. Boss, R.B. Pilz, Pro-survival effects of 17β-estradiol on osteocytes are mediated by nitric oxide/cGMP via differential actions of cGMP-dependent protein kinases I and II, J. Biol. Chem. 287 (2) (2012) 978–988.
[25] H. Kalyanaraman, G. Schwaerzer, G. Ramdani, F. Castillo, B.T. Scott, W. Dillmann, R.L. Sah, D.E. Casteel, R.B. Pilz, Protein kinase G activation reverses oxidative stress and restores osteoblast function and bone formation in male mice with type 1 diabetes, Diabetes 67 (4) (2018) 607–623.
[26] H. Kalyanaraman, S. Pal China, J.A. Cabriales, J. Moininazeri, D.E. Casteel, J. J. Garcia, V.W. Wong, A. Chen, R.L. Sah, G.R. Boss, R.B. Pilz, Protein kinase G2 is essential for skeletal homeostasis and adaptation to mechanical loading in male but not female mice, J. Bone Miner. Res. : the official journal of the American Society for Bone and Mineral Research 38 (1) (2023) 171–185.
[27] N. Schall, J.J. Garcia, H. Kalyanaraman, S.P. China, J.J. Lee, R.L. Sah, A. Pfeifer, R. B. Pilz, Protein kinase G1 regulates bone regeneration and rescues diabetic fracture healing, JCI insight 5 (9) (2020).
[28] S. Sortino, Light-controlled nitric oxide delivering molecular assemblies, Chem. Soc. Rev. 39 (8) (2010) 2903–2913.
[29] M.C. Jen, M.C. Serrano, R. van Lith, G.A. Ameer, Polymer-based nitric oxide therapies: recent insights for biomedical applications, Adv. Funct. Mater. 22 (2) (2012) 239–260.
[30] L. Yang, E.S. Feura, M.J.R. Ahonen, M.H. Schoenfisch, Nitric oxide-releasing macromolecular scaffolds for antibacterial applications, Adv. Healthcare Mater. 7 (13) (2018) e1800155.
[31] S. Perrin, C. Colnot, Periosteal skeletal stem and progenitor cells in bone regeneration, Curr. Osteoporos. Rep. 20 (5) (2022) 334–343.
[32] J. Pajarinen, T. Lin, E. Gibon, Y. Kohno, M. Maruyama, K. Nathan, L. Lu, Z. Yao, S. B. Goodman, Mesenchymal stem cell-macrophage crosstalk and bone healing, Biomaterials 196 (2019) 80–89.
[33] Y. Niu, Z. Wang, Y. Shi, L. Dong, C. Wang, Modulating macrophage activities to promote endogenous bone regeneration: biological mechanisms and engineering approaches, Bioact Mater 6 (1) (2021) 244–261.
[34] J. Zhang, J. Pan, W. Jing, Motivating role of type H vessels in bone regeneration, Cell Prolif. 53 (9) (2020) e12874.
[35] S. Kuttappan, D. Mathew, J.I. Jo, R. Tanaka, D. Menon, T. Ishimoto, T. Nakano, S. V. Nair, M.B. Nair, Y. Tabata, Dual release of growth factor from nanocomposite fibrous scaffold promotes vascularisation and bone regeneration in rat critical sized calvarial defect, Acta Biomater. 78 (2018) 36–47.
[36] K.K. Sivaraj, R.H. Adams, Blood vessel formation and function in bone, Development 143 (15) (2016) 2706–2715.
[37] D.S. Sparks, F.M. Savi, S. Saifzadeh, M.A. Schuetz, M. Wagels, D.W. Hutmacher, Convergence of scaffold-guided bone reconstruction and surgical vascularization strategies-A quest for regenerative matching axial vascularization, Front. Bioeng. Biotechnol. 7 (2019) 448.
[38] K. Hu, B.R. Olsen, The roles of vascular endothelial growth factor in bone repair and regeneration, Bone 91 (2016) 30–38.
[39] H. Matsubara, D.E. Hogan, E.F. Morgan, D.P. Mortlock, T.A. Einhorn, L. C. Gerstenfeld, Vascular tissues are a primary source of BMP2 expression during bone formation induced by distraction osteogenesis, Bone 51 (1) (2012) 168–180.
[40] Y. Baldik, A.D. Diwan, R.C. Appleyard, Z.M. Fang, Y. Wang, G.A. Murrell, Deletion of iNOS gene impairs mouse fracture healing, Bone 37 (1) (2005) 32–36.
[41] P. Collin-Osdoby, L. Rothe, S. Bekker, F. Anderson, P. Osdoby, Decreased nitric oxide levels stimulate osteoclastogenesis and bone resorption both in vitro and in vivo on the chick chorioallantoic membrane in association with neoangiogenesis, J. Bone Miner. Res. : the official journal of the American Society for Bone and Mineral Research 15 (3) (2000) 474–488.

[42] J. Aguirre, L. Buttery, M. O'Shaughnessy, F. Afzal, I. Fernandez de Marticorena, M. Hukkanen, P. Huang, I. MacIntyre, J. Polak, Endothelial nitric oxide synthase gene-deficient mice demonstrate marked retardation in postnatal bone formation, reduced bone volume, and defects in osteoblast maturation and activity, Am. J. Pathol. 158 (1) (2001) 247–257.
[43] B.B. Yaroslavskiy, I. Turkova, Y. Wang, L.J. Robinson, H.C. Blair, Functional osteoclast attachment requires inositol-1,4,5-trisphosphate receptor-associated cGMP-dependent kinase substrate, Laboratory investigation; a journal of technical methods and pathology 90 (10) (2010) 1533–1542.
[44] S. Pal China, H. Kalyanaraman, S. Zhuang, J.A. Cabriales, R.L. Sah, R.B. Pilz, Protein kinase G2 activation restores Wnt signaling and bone mass in glucocorticoid-induced osteoporosis in mice, JCI insight (2024).
[45] Z. Jin, J. Kho, B. Dawson, M.M. Jiang, Y. Chen, S. Ali, L.C. Burrage, M. Grover, D. J. Palmer, D.L. Turner, P. Ng, S.C. Nagamani, B. Lee, Nitric oxide modulates bone anabolism through regulation of osteoblast glycolysis and differentiation, J. Clin. Invest. 131 (5) (2021).
[46] C. Ruan, N. Hu, Y. Ma, Y. Li, J. Liu, X. Zhang, H. Pan, The interfacial pH of acidic degradable polymeric biomaterials and its effects on osteoblast behavior, Sci. Rep. 7 (1) (2017) 6794.
[47] K. Lavanya, S.V. Chandran, K. Balagangadharan, N. Selvamurugan, Temperature- and pH-responsive chitosan-based injectable hydrogels for bone tissue engineering, Materials science & engineering, C, Materials for biological applications 111 (2020) 110862.
[48] Y. Hazehara-Kunitomo, E.S. Hara, M. Ono, K.T. Aung, K. Komi, H.T. Pham, K. Akiyama, M. Okada, T. Oohashi, T. Matsumoto, T. Kuboki, Acidic pre-conditioning enhances the stem cell phenotype of human bone marrow stem/progenitor cells, Int. J. Mol. Sci. 20 (5) (2019).
[49] B. Bisht, A. Hope, A. Mukherjee, M.K. Paul, Advances in the fabrication of scaffold and 3D printing of biomimetic bone graft, Ann. Biomed. Eng. 49 (4) (2021) 1128–1150.
[50] A. Oryan, S. Sahvieh, Effectiveness of chitosan scaffold in skin, bone and cartilage healing, Int. J. Biol. Macromol. 104 (Pt A) (2017) 1003–1011.
[51] A. Wubneh, E.K. Tsekoura, C. Ayranci, H. Uludağ, Current state of fabrication technologies and materials for bone tissue engineering, Acta Biomater. 80 (2018) 1–30.
[52] J. Deng, J. Pan, X. Han, L. Yu, J. Chen, W. Zhang, L. Zhu, W. Huang, S. Liu, Z. You, Y. Liu, PDGFBB-modified stem cells from apical papilla and thermosensitive hydrogel scaffolds induced bone regeneration, Chem. Biol. Interact. 316 (2020) 108931.
[53] M. Liu, X. Zeng, C. Ma, H. Yi, Z. Ali, X. Mou, S. Li, Y. Deng, N. He, Injectable hydrogels for cartilage and bone tissue engineering, Bone Res 5 (2017) 17014.
[54] Y. Chen, W. Sheng, J. Lin, C. Fang, J. Deng, P. Zhang, M. Zhou, P. Liu, J. Weng, F. Yu, D. Wang, B. Kang, H. Zeng, Magnesium oxide nanoparticle coordinated phosphate-functionalized chitosan injectable hydrogel for osteogenesis and angiogenesis in bone regeneration, ACS Appl. Mater. Interfaces 14 (6) (2022) 7592–7608.
[55] M. Bhattacharjee, J.L. Escobar Ivirico, H.M. Kan, S. Shah, T. Otsuka, R. Bordett, M. Barajaa, N. Nagiah, R. Pandey, L.S. Nair, C.T. Laurencin, Injectable amnion hydrogel-mediated delivery of adipose-derived stem cells for osteoarthritis treatment, Proc. Natl. Acad. Sci. U. S. A. 119 (4) (2022).
[56] M.M. Hasani-Sadrabadi, P. Sarrion, S. Pouraghaei, Y. Chau, S. Ansari, S. Li, T. Aghaloo, A. Moshaverinia, An engineered cell-laden adhesive hydrogel promotes craniofacial bone tissue regeneration in rats, Sci. Transl. Med. 12 (534) (2020).
[57] H. Zhang, S. Wu, W. Chen, Y. Hu, Z. Geng, J. Su, Bone/cartilage targeted hydrogel: strategies and applications, Bioact Mater 23 (2023) 156–169.
[58] L. Bai, G. Tao, M. Feng, Y. Xie, S. Cai, S. Peng, J. Xiao, Hydrogel drug delivery systems for bone regeneration, Pharmaceutics 15 (5) (2023).
[59] J. Liu, L. Yang, K. Liu, F. Gao, Hydrogel scaffolds in bone regeneration: their promising roles in angiogenesis, Front. Pharmacol. 14 (2023) 1050954.
[60] L. Soundararajan, A. Dharmarajan, P. Samji, Regulation of pleiotropic physiological roles of nitric oxide signaling, Cell. Signal. 101 (2023) 110496.
[61] B. Bonavida, H. Garban, Nitric oxide-mediated sensitization of resistant tumor cells to apoptosis by chemo-immunotherapeutics, Redox Biol. 6 (2015) 486–494.
[62] R. González, F.J. Molina-Ruiz, J.A. Bárcena, C.A. Padilla, J. Muntané, Regulation of cell survival, apoptosis, and epithelial-to-mesenchymal transition by nitric oxide-dependent post-translational modifications, Antioxidants Redox Signal. 29 (13) (2018) 1312–1332.